

JAX-MPM: A Learning-Augmented Differentiable Meshfree Framework for GPU-Accelerated Lagrangian Simulation and Geophysical Inverse Modeling

Honghui Du^a, QiZhi He^{a,*}

^a*Department of Civil, Environmental, and Geo- Engineering, University of Minnesota, 500 Pillsbury Drive S.E., Minneapolis, MN 55455*

Abstract

Differentiable programming that enables automatic differentiation through simulation pipelines has emerged a powerful paradigm in scientific computing, naturally supporting forward and inverse modeling and facilitating seamless integration with deep learning frameworks. In this study, we present JAX-MPM, a general-purpose differentiable meshfree solver within a hybrid Lagrangian–Eulerian framework, tailored specifically for simulating complex continuum mechanics problems involving large deformations, frictional contact, and inelastic material behavior, with particular emphasis on geomechanics and geophysical hazard applications. The proposed theoretical framework is built upon the material point method (MPM) and implemented in the modern JAX computing architecture, resulting in a fully differentiable simulator. Leveraging high-performance GPU computing, this framework supports efficient gradient-based optimization directly through its time-stepping solvers, enabling high-fidelity forward and inverse modeling of large-scale continuum systems. Moreover, JAX-MPM inherently supports the joint training of physical models and neural networks, allowing the learning of embedded hidden system closures or constitutive models parameterized by neural networks. We validate the JAX-MPM framework through a series of 2D and 3D benchmark simulations, including dam-breaks and granular collapses, demonstrating its numerical accuracy and GPU-accelerated performance. We show that a high-resolution 3D simulation of a granular cylinder collapse with 2.7 million particles completes 1000 time steps in around 22 seconds (single precision) and 98 seconds (double precision) on a single GPU. Beyond forward modeling, we demonstrate inverse modeling capabilities through applications such as velocity field reconstruction and spatially varying friction estimation. Collectively, these results establish JAX-MPM as a unified and scalable platform for differentiable meshfree modeling, advancing data assimilation and physical inference for complex solid and geophysical applications.

*Corresponding author
Email address: qzhe@umn.edu (QiZhi He)

Keywords: Differentiable programming, Lagrangian meshfree formulation, MPM, Geophysical hazards, Inverse modeling, Scientific machine learning, JAX

1. Introduction

1.1. Overview

Natural hazards or geohazards [36, 46]—such as landslides, dam-breaks, debris flows, and soil liquefaction—are commonly recognized as gravitationally-driven processes, which involve large-scale failure of geomaterials (e.g., soils, rocks, and granular media that constitute the Earth’s near-surface), posing substantial risks to both natural and built environments. These phenomena are governed by highly nonlinear, path-dependent material behavior [95], and typically involve severe deformations and rapidly evolving boundary conditions [4], making predictive high-fidelity modeling and simulation of such hazard processes extremely challenging.

Numerical simulation has become a cornerstone of computational geomechanics, playing a critical role in geotechnical prediction and geohazard mitigation by enabling the analysis of complex geophysical processes primarily governed by partial differential equations (PDEs). Mesh-based methods such as the finite element method (FEM) [76, 61, 93] and finite volume method (FVM) [30, 29] have been widely adopted for this purpose. For example, FEM has been applied to simulate flow-like landslides [24], while FVM has been used to model coupled flow and shear failure in fractured geomechanical systems [29]. These methods have provided valuable insights in geohazard research and remain effective for problems involving moderate deformation and well-defined boundaries. However, in geohazard modeling scenarios characterized by extreme deformation, fragmentation, and evolving topologies, mesh-based methods often face numerical challenges due to severe mesh distortion and tangling, and can become unreliable or computationally impractical. To address these limitations, meshfree methods have been developed, representing materials as collections of particles or discrete points—eliminating the need for conforming meshes and improving robustness in large-deformation problems.

Another critical challenge in geomechanical modeling is the limited observability of real-world systems. For instance, essential quantities, such as initial velocity fields, internal stress states, and spatially varying friction, are usually unknown or unmeasurable in situ. Therefore, inverse modeling becomes essential in these cases, enabling the estimation of latent physical parameters from partial observations [17, 1], to improve predictive accuracy and support real-world risk assessment and design. Conventional approaches typically rely on repeated forward simulations within optimization loops, including probabilistic methods such as Bayesian inference with Gaussian processes [103] and Markov chain Monte Carlo (MCMC) methods [20]. While these offer uncertainty quantification, they are computationally expensive and difficult to scale in high-dimensional, nonlinear systems. Gradient-based alternatives such as adjoint solvers improve

efficiency, but are often impractical to implement for systems with contact, friction, and path-dependent materials.

Altogether, the above-mentioned challenges highlight the need for a fundamentally novel simulation framework that integrates high-fidelity physical models, capable of capturing complex deformation and material inelasticity, with inverse modeling capability.

1.2. Lagrangian meshfree simulation

Meshfree methods provide a robust foundation for handling large deformations and dynamic boundary conditions, as they naturally avoid mesh entanglement and eliminate the need for frequent remeshing [18]. Prominent examples include Smoothed Particle Hydrodynamics (SPH) [37, 67], the Discrete Element Method (DEM) [26, 25], and the Material Point Method (MPM) [90, 91, 60]. These methods commonly utilize a Lagrangian formulation, in which computational particles move with the material, explicitly carrying essential state variables such as stress, strain, and internal history variables. This particle-based representation inherently supports accurate tracking of material evolution and path-dependent behavior, which is crucial for capturing complex phenomena in geomechanical simulations.

Among these methods, the Material Point Method (MPM) stands out due to its hybrid Eulerian–Lagrangian formulation. In this approach, material points carry internal state variables and track continuum deformation in a Lagrangian manner, while computational operations are performed on a background Eulerian grid that is reset at each time step. This decoupling of material and computational domains offers notable advantages [28], including avoiding mesh distortion and efficiently handling complex contact and costly particle–particle interactions via the background grid. These attributes make MPM particularly attractive for modeling challenging geomechanical problems [8, 3, 5] such as landslides, debris flows, and multiphase failure, where large deformations, fragmentation, and multi-body interactions are dominant. Given these strengths, MPM is adopted as the computational foundation for the differentiable simulation framework developed in this study.

1.3. Machine learning and differentiable simulators in geomechanics

To address the challenges of inverse modeling in geophysical hazards, where traditional methods often face limitations in efficiency and scalability, we explore differentiable programming as a flexible and scalable alternative. Differentiable programming (DP) [54, 77, 12] enables end-to-end gradient computation through entire simulation pipelines using automatic differentiation (AD) [9]. Unlike sampling-based or adjoint-based approaches, DP avoids the need for manual derivations and naturally supports optimization over both physical parameters and latent states, even in systems with complex dynamics.

DP-based methods can be broadly categorized according to how differentiability is achieved—either through continuous formulations or discretized numerical solvers. The first category leverages neural networks (NNs) to achieve differentiability, for example, by embedding physical laws into network architectures or

learning system dynamics directly from data using neural operators (also known as emulators). The second approach builds on established numerical solvers, which are made differentiable through modern AD frameworks, allowing efficient gradient computation with respect to simulation inputs or model parameters in an end-to-end manner.

1.3.1. Continuous approach: Neural network based methods

Neural networks have become widely used in physics-based modeling, offering differentiable approximations to PDE solutions suitable for both forward and inverse problems. A prominent approach is physics-informed neural networks (PINNs) [78], which explicitly enforce governing equations through their loss functions to guide the learning process. Owing to their architectural flexibility, PINNs have been applied across a wide range of engineering and scientific disciplines [27], including fluid mechanics [79, 16], solid mechanics [39, 38, 80], subsurface transport [41, 34]. However, PINNs often suffer from gradient flow pathologies [94] and high computational cost due to the evaluation of high-order derivatives [33]. These challenges have spurred the development of hybrid neural–numerical approaches, which integrate discrete approximations into the PINN framework to improve accuracy and efficiency [33]. Despite these advances, the practical application of PINNs in geomechanics and geophysical modeling remains limited, largely due to the added complexity of inelastic material behavior and multiphysics coupling [100].

Another notable approach to modeling physical systems with neural networks is to build data-driven surrogates, such as emulators or neural operators, which learn system dynamics directly from observational data. These surrogates leverage a range of architectures, including graph neural networks (GNNs) [81], MeshGraphNet [75], Fourier neural operators (FNO) [65], and DeepONet [68]. Recently, a hybrid framework coupling neural operators with the classical FEM has been introduced for solid mechanics [99] and geophysical modeling [42], further enhancing the integration of data-driven models with traditional numerical methods.

In Lagrangian (particle-based) settings, GNN-based simulators are commonly used to model local interactions by dynamically constructing neighborhoods of particles [2, 21]. While these methods are very expressive, they often suffer from high computational costs due to repeated neighbor searches and can face scalability challenges. To mitigate these issues, a hybrid Eulerian–Lagrangian design has been proposed [62, 83] in which particle states are projected onto a background grid via particle-to-grid (P2G) transfers, evolved using grid-based convolutional neural networks (CNNs), and then mapped back to particles using grid-to-particle (G2P) operations. This structure avoids explicit neighbor searches and supports more scalable training. Despite these innovations, such learned neural simulators remain purely data-driven. They rely heavily on training data, do not explicitly enforce physical laws, and often generalize poorly outside the training distribution, especially in long-term or multiphysics scenarios.

1.3.2. Discrete approach: differentiable physics solver

To circumvent the limitations of neural network-based approaches, increasing attention has been directed toward the second category: high-fidelity differentiable physics solvers, also referred to as differentiable simulators [82, 72]. These simulators bridge the gap between classical physics-based modeling and end-to-end learning by constructing solvers that are natively compatible with AD frameworks [9], thereby allowing direct gradient computations through the entire simulation time-stepping process. As a result, differentiable simulators provide a physically consistent and scalable foundation for inverse modeling, without requiring pre-training or manual derivation of adjoint equations. By supporting gradient-based optimization with respect to material properties, initial conditions, and control inputs, differentiable simulators enable a wide range of applications including system identification [66], trajectory and policy optimization [51, 19], and material design problems [96, 98, 48].

In this work, we focus specifically on the differentiable implementation of MPM, which is inherently well-suited for modeling large deformation processes in geophysical systems. Traditional MPM implementations are typically developed in imperative programming languages such as C++ [60], Fortran [102], or high-level scientific computing platforms like Julia [86, 53]. While these implementations are efficient and widely used for forward simulations, they are not inherently designed to support differentiability or seamless integration with AD-based deep learning frameworks. Recent efforts have explored differentiable MPM solvers implemented in Taichi [50], a domain-specific programming language featuring built-in AD capacities [49]. Taichi has been successfully employed in various applications, including physics-based modeling and computer graphics [50, 49, 85], as well in tasks involving parameter and system identification [64, 97]. Despite these advances in MPM implementations, their development specifically tailored for large-scale, differentiable geomechanical modeling remains rare. Key limitations of existing approaches include restricted autodiff flexibility, limited multi-GPU support, and a separation between simulation and machine learning components.

These limitations highlight a critical need for developing a fully differentiable Lagrangian simulator for high-fidelity geomechanical simulations, enabling a unified framework for scalable forward and inverse modeling workflows.

1.4. A learning-based meshfree computational framework

To address this gap, we propose a general-purpose, Lagrangian meshfree solver built on JAX [14], a modern computational backend specifically tailored for differentiable programming. JAX integrates automatic differentiation, just-in-time (JIT) compilation, and GPU/TPU acceleration through the Accelerated Linear Algebra (XLA) compiler. Unlike imperative programming frameworks, which typically require explicit control over memory and execution flow, JAX promotes a functional, vectorized programming style, enabling efficient, loop-free simulations fully compatible with gradient-based optimization. Additionally, JAX integrates seamlessly with modern deep learning libraries such as Flax [43],

Haiku [44], and Equinox [56], supporting the joint training of physical models and neural networks. JAX’s built-in parallelization tools, such as `vmap` and `pmap`, further facilitate efficient multi-GPU computation and batched operations, essential for large-scale inverse modeling and data-driven geomechanical workflows. Recently, JAX has been effectively combined with canonical numerical methods, such as FEM [98], finite difference method [69], finite-volume CFD solver [11], SPH [92] and meshless local Petrov-Galerkin method [32], among others.

Leveraging these capabilities, we develop JAX-MPM in this study, a GPU-accelerated, fully differentiable Material Point Method framework for large-deformation simulation and inverse modeling in geomechanics and solid mechanics. Implemented entirely in JAX, it unifies simulation, automatic differentiation, and neural networks within a single system, eliminating the need for external toolchains or inter-language bindings required by Taichi-based approaches. By combining the physical rigor of MPM with JAX’s flexibility, JAX-MPM enables robust, end-to-end pipelines for forward simulation, gradient-based inversion, and learning-driven optimization in natural hazard analysis and related applications.

We evaluate the effectiveness of JAX-MPM through a diverse set of benchmark problems representative of real-world geomechanical systems. These include both 2D and 3D dam-break scenarios and granular collapses, where the simulator accurately captures large deformations, free-surface evolution, and interactions with rigid boundaries. We also highlight the computational advantages of JAX-MPM through efficient GPU acceleration. For example, JAX-MPM completes 1000 time steps in approximately 8.2 seconds for a 3D dam-break simulation with 1.9 million particles on a $200 \times 100 \times 80$ grid, and around 22 seconds for a granular cylinder collapse with 2.7 million particles on a $400 \times 400 \times 100$ grid, both using single precision on a single GPU.

For inverse modeling, JAX-MPM introduces a unified PDE-constrained optimization framework that accommodates both Lagrangian (particle-based) and Eulerian (region-based) supervision without modifying the simulation pipeline. This flexible formulation allows integration of diverse observational inputs, such as sparse particle trajectories or fixed-location velocity sensors. We demonstrate its effectiveness on representative inverse tasks including initial velocity reconstruction and spatially varying friction estimation. These tasks span up to $\mathcal{O}(10^3)$ trainable parameters and $\mathcal{O}(10^4)$ degrees of freedom. In all cases, JAX-MPM achieves accurate, physically consistent reconstructions using only partial observational data, underscoring its potential for real-world geohazard applications.

1.5. Aims and structure

The main contributions of this work are summarized as follows: 1) develop JAX-MPM, a *fully differentiable GPU-accelerated meshfree solver* for high-fidelity geomechanical simulations; 2) introduce a *unified inverse modeling framework* supporting both Lagrangian (particle-based) and Eulerian (region-based) data, enabling flexible and scalable inference of physical parameters from diverse observational sources; and 3) demonstrate the potential of JAX-MPM for hy-

brid physics–machine learning workflows, facilitating end-to-end differentiable pipelines for parameter estimation and field reconstruction.

The remainder of the paper is organized as follows. Section 2 introduces the physical modeling and numerical formulation of the Material Point Method employed in JAX-MPM. Section 3 details the implementation of scalable inverse modeling within the JAX-MPM framework. Section 4 presents forward simulation results for representative benchmark problems. Section 5 demonstrates inverse modeling capabilities, including parameter estimation and field reconstruction. Finally, Section 6 concludes the paper with a summary and future directions.

2. Preliminary

In this section, we briefly review the governing equations and explicit time integration scheme underlying the proposed differentiable meshfree framework based on MPM, as detailed in Sections 2.1 and 2.2. We then introduce several classical constitutive material models employed in this study (Sections 2.3).

2.1. Governing equations

The balance of linear momentum in the Lagrangian (material) frame, defined over a domain $\Omega \subset \mathbb{R}^d$, where d is the spatial dimension and $t \in [0, T]$, is given by:

$$\begin{cases} \rho \dot{\mathbf{v}} = \nabla \cdot \boldsymbol{\sigma} + \rho \mathbf{b}, \\ \boldsymbol{\sigma} \cdot \mathbf{n} = \bar{\mathbf{t}} \quad \text{on } \Gamma_N, \\ \mathbf{u} = \bar{\mathbf{u}} \quad \text{on } \Gamma_D, \end{cases} \quad (1)$$

where ρ denotes the material density, \mathbf{b} is the body force per unit mass, and $\boldsymbol{\sigma}$ is the Cauchy stress tensor. The boundary $\partial\Omega$ is partitioned into Dirichlet (Γ_D) and Neumann (Γ_N) portions, corresponding to prescribed displacements and tractions, respectively. The velocity field is defined as $\mathbf{v} = \dot{\mathbf{u}}$, where \mathbf{u} is the displacement field. Material time derivatives relate the kinematic quantities by $\mathbf{a} = \dot{\mathbf{v}} = \ddot{\mathbf{u}}$, with all derivatives taken following the material motion.

The weak form of Eq. (1) is derived by multiplying with a test function \mathbf{w} , integrating over the current configuration, and applying the divergence theorem:

$$\int_{\Omega} \mathbf{w} \cdot \rho \mathbf{a} \, d\Omega = - \int_{\Omega} \nabla \mathbf{w} : \boldsymbol{\sigma} \, d\Omega + \int_{\Omega} \mathbf{w} \cdot \rho \mathbf{b} \, d\Omega + \int_{\Gamma_N} \mathbf{w} \cdot \bar{\mathbf{t}} \, d\Gamma \quad (2)$$

where \mathbf{w} vanishes on Γ_D .

Following the standard Material Point Method (MPM) framework [90, 91], the continuum domain is discretized using a set of material points (also referred to as particles) located at positions \mathbf{x}_p , for $p = 1, \dots, N_p$, which move freely over a fixed background Cartesian grid (illustrated in Fig. 1). Each material point represents a subdomain $\Omega_p \subset \Omega$, and carries the physical properties of the continuum, such as mass, volume, velocity, and stress. This particle-based

discretization allows us to rewrite the weak form of the momentum balance equation (2) as a sum over all material points:

$$\sum_p \int_{\Omega_p} \mathbf{w} \cdot \rho \mathbf{a} \, d\Omega = - \sum_p \int_{\Omega_p} \nabla \mathbf{w} : \boldsymbol{\sigma} \, d\Omega + \sum_p \int_{\Omega_p} \mathbf{w} \cdot \rho \mathbf{b} \, d\Omega + \sum_p \int_{\Gamma_N} \mathbf{w} \cdot \bar{\mathbf{t}} \, d\Gamma \quad (3)$$

where the index p denotes the material points in the domain. Note that the conservation of mass is inherently satisfied in the MPM formulation and is therefore omitted from this derivation [90].

To interpolate field variables onto the background grid, we introduce finite element (FE)-based nodal interpolation:

$$\mathbf{a} = \sum_i \phi_i(\mathbf{x}) \mathbf{a}_i, \quad \mathbf{w} = \sum_i \phi_i(\mathbf{x}) \mathbf{w}_i \quad (4)$$

where the index i denotes summation over over all N_g grid nodes, and $\phi_i(\mathbf{x})$ is the shape function associated with node i . In this study, we employ a quadratic B-spline basis function $w(\xi)$ [88], defined as

$$\omega(\xi) = \begin{cases} -|\xi|^2 + \frac{3}{4} & 0 \leq |\xi| < \frac{1}{2} \\ \frac{1}{2}|\xi|^2 - \frac{3}{2}|\xi| + \frac{9}{8} & \frac{1}{2} \leq |\xi| < \frac{3}{2} \\ 0 & \frac{3}{2} \leq |\xi| \end{cases} \quad (5)$$

The multidimensional shape function $\phi_i(\mathbf{x})$ is constructed using a tensor product of one-dimensional B-splines:

$$\phi_i(\mathbf{x}) = \prod_{\alpha=1}^d \omega\left(\frac{x_\alpha - x_{i\alpha}}{\Delta h}\right) \quad (6)$$

where Δh is the uniform grid spacing.

Substituting Eq. (4) into the discrete weak form and considering the arbitrariness of \mathbf{w}_i , we obtain the semi-discrete form:

$$\sum_{j=1}^{N_g} m_{ij} \mathbf{a}_j = \mathbf{f}_i^{\text{int}} + \mathbf{f}_i^{\text{ext}} \quad (7)$$

where

$$\begin{aligned} m_{ij} &= \sum_p \int_{\Omega_p} \phi_i \phi_j \rho \, d\Omega = \sum_p m_p \phi_{ip} \phi_{jp} \\ \mathbf{f}_i^{\text{int}} &= - \sum_p \int_{\Omega_p} \nabla \phi_i \cdot \boldsymbol{\sigma} \, d\Omega = - \sum_p V_p \nabla \phi_{ip} \cdot \boldsymbol{\sigma}_p \\ \mathbf{f}_i^{\text{ext}} &= \sum_p \left[\int_{\Omega_p} \phi_i \rho \mathbf{b} \, d\Omega + \int_{\Gamma_N} \phi_i \bar{\mathbf{t}} \, d\Gamma \right] = \sum_p \phi_{ip} m_p \mathbf{b}_p + \bar{\mathbf{f}}_i \end{aligned} \quad (8)$$

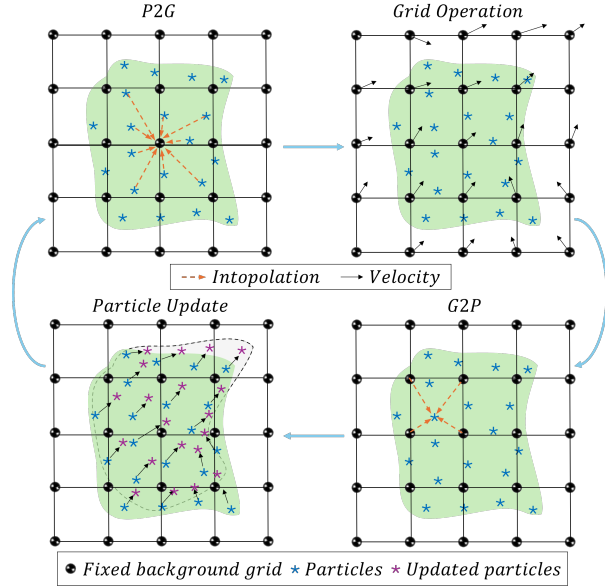


Figure 1: Illustration of the Material Point Method (MPM) procedure. The procedure consists of four stages: P2G transfer, grid based operations, G2P transfer, and particle state update. Black dots denote the fixed background grid, blue stars represent particles, and purple stars indicate updated particles. Dashed orange arrows illustrate interpolation contributions, while solid black arrows indicate velocity vectors.

where $\phi_{ip} = \phi_i(\mathbf{x}_p)$, and m_p is the mass of particle p . m_{ij} is the consistent mass matrix. In this study, we adopt a lumped mass matrix, i.e., $m_i \equiv m_{ii} = \sum_p m_p \phi_{ip}$, to avoid an expensive matrix inversion [90]. Applying explicit time discretization, the semi-discrete momentum equation (8) becomes:

$$m_i^n \frac{\mathbf{v}_i^{n+1} - \mathbf{v}_i^n}{\Delta t} = \mathbf{f}_i^{\text{int},n} + \mathbf{f}_i^{\text{ext},n} := \mathbf{f}_i^n \quad (9)$$

where forward Euler integration is used for simplicity and efficiency. Here, $\mathbf{f}_i^n = \mathbf{f}_i^{\text{int},n} + \mathbf{f}_i^{\text{ext},n}$ is the total force acting on node i at time step n , consisting of internal and external contributions. The superscript n indicates the current time step, and $\Delta t = t^{n+1} - t^n$ is the time increment. To ensure the numerical stability of the explicit scheme, Δt is determined according to the Courant–Friedrichs–Lewy (CFL) condition [23].

2.2. Implementation of material point method

As shown in Fig. 1, each time step in the MPM solution procedure consists of three computational stages: particle-to-grid (P2G) transfer, grid-based updates, and grid-to-particle (G2P) transfer. These stages are described in detail below.

2.2.1. Particle-to-grid transfer

In the P2G phase, particle information is projected onto the background grid using interpolation kernels. The mass at grid node i is computed via a weighted sum over particles

$$m_i^n = \sum_p m_p \phi_{ip}^n. \quad (10)$$

The momentum contributions from particles are aggregated to compute the grid velocity:

$$\mathbf{v}_i^n = \frac{1}{m_i^n} \sum_p m_p \phi_{ip}^n \mathbf{v}_p^n. \quad (11)$$

The nodal force \mathbf{f}_i^n includes internal stresses, body forces, and externally applied forces:

$$\mathbf{f}_i^n = - \sum_p V_p^n \nabla \phi_{ip}^n \cdot \boldsymbol{\sigma}_p^n + \sum_p \phi_{ip}^n m_p \mathbf{b}_p + \bar{\mathbf{f}}_i, \quad (12)$$

where V_p^n and $\boldsymbol{\sigma}_p^n$ are the volume and stress of particle p , \mathbf{b}_p is the body force per unit mass, and $\bar{\mathbf{f}}_i$ represents externally applied nodal forces, defined in Eq. (8).

2.2.2. Grid velocity update

With the nodal masses and forces being obtained, the grid acceleration is calculated using Newton's second law:

$$\mathbf{a}_i^n = \frac{\mathbf{f}_i^n}{m_i^n}. \quad (13)$$

The grid velocity is then updated using an explicit time integration scheme:

$$\mathbf{v}_i^{n+1} = \mathbf{v}_i^n + \Delta t \mathbf{a}_i^n. \quad (14)$$

Boundary conditions are imposed explicitly on the grid. For instance, to enforce a fixed (Dirichlet) boundary condition on a set of nodes Γ_D , we impose

$$\mathbf{a}_i^n = \mathbf{0}, \quad \mathbf{v}_i^n = \mathbf{0}, \quad \text{for } i \in \Gamma_D.$$

2.2.3. Grid-to-particle transfer

Following the update of grid velocities, information is transferred back to the particles to advance the simulation. JAX-MPM supports several established transfer schemes, including fluid-implicit particle (FLIP) [13], particle-in-cell (PIC) [40], affine-PIC (APIC) [55] and Taylor-PIC (PIC) [71]. In this section, we describe the commonly used FLIP and PIC methods, additional variants are detailed in Appendix B.

The FLIP scheme updates the particle velocity using the grid acceleration:

$$\mathbf{v}_p^{n+1} = \mathbf{v}_p^n + \Delta t \sum_i \phi_{ip}^n \mathbf{a}_i^n. \quad (15)$$

Alternatively, the PIC scheme directly interpolates the updated grid velocity

$$\mathbf{v}_p^{n+1} = \sum_i \phi_{ip}^n \mathbf{v}_i^{n+1}. \quad (16)$$

PIC replaces the particle velocity with the interpolated grid velocity, introducing numerical dissipation into the system [40]. In constrst, FLIP only adds the increment of grid velocity, which preserves particle-level quantities and reduces numerical dissipation, but may introduce noise and instability [13, 28]. To balance these effects, a blended scheme [104] can be used.

The particle position is updated using the nodal velocity field:

$$\mathbf{x}_p^{n+1} = \mathbf{x}_p^n + \Delta t \sum_i \phi_{ip}^n \mathbf{v}_i^{n+1}, \quad (17)$$

and the velocity gradient at each particle is evaluated by:

$$\nabla \mathbf{v}_p^{n+1} = \sum_i \mathbf{v}_i^{n+1} \otimes \nabla \phi_{ip}^n. \quad (18)$$

Together, these three stages complete one full MPM time step and constitute the core computational cycle of the JAX-MPM framework.

Remark 1 (Stress Update Schemes). A critical aspect of MPM implementation is the choice of stress update scheme, which defines when stresses are evaluated relative to the solution of the momentum equation. Two common stress update schemes in MPM are *Update Stress Last (USL)* and *Update Stress First (USF)* [7]. USL updates stresses after computing internal forces and advancing velocities, offering better stability and modularity. USF updates stresses earlier, during the P2G step, which can improve energy conservation but may be less stable in dynamic problems. The implementation described above follows the USL approach. The specific stress update procedure is detailed in the next section.

2.3. Constitutive model

JAX-MPM supports constitutive models tailored for large-deformation geophysical simulations. In this study, we consider two representative materials: (1) Newtonian fluids, which are employed in dam-break scenarios, and (2) elastoplastic constitutive model with Drucker–Prager yield criterion, widely employed to capture shear and tensile failure in granular materials. The stress update procedures for each materiel models are detailed below.

- For the Newtonian fluid model, the Cauchy stress tensor $\boldsymbol{\sigma}_p^{n+1}$ is updated as

$$\boldsymbol{\sigma}_p^{n+1} = -p_p^{n+1} \mathbf{I} - \frac{2}{3} \mu \text{tr}(\Delta \mathbf{d}_p) \mathbf{I} + 2\mu \Delta \mathbf{d}_p, \quad (19)$$

where \mathbf{d}_p represents the rate of deformation tensor, and $\Delta \mathbf{d}_p = \frac{1}{2}(\nabla \mathbf{v}_p^{n+1} + \nabla^\top \mathbf{v}_p^{n+1})\Delta t$, \mathbf{I} is the identity tensor, and μ is the dynamic viscosity.

To model incompressibility, we adopt a weakly compressible formulation, where the pressure is computed using an artificial equation of state (EOS) [58, 63, 70]

$$p_p^{n+1} = c_n^2(\rho_p^{n+1} - \rho_0) \quad (20)$$

where c_n is the numerical sound speed, ρ_0 is the reference density of fluid, and ρ_p^{n+1} is the updated fluid density at time step $(n + 1)$, computed as $\rho_p^{n+1} = \rho_p^n / (1 + \det(\Delta \mathbf{d}_p))$.

- For granular flow simulations, we adopt a non-associated Drucker–Prager (D-P) plasticity model with a tension cutoff, following [52, 73]. To maintain objectivity under large deformation, the Jaumann stress rate is used. Thus, the stress is updated by:

$$\boldsymbol{\sigma}_p^{n+1} = \boldsymbol{\sigma}_p^n + \boldsymbol{\sigma}_p^{\nabla J} \Delta t + (\Delta \boldsymbol{\omega}_p \cdot \boldsymbol{\sigma}_p^n + \boldsymbol{\sigma}_p^n \cdot \Delta \boldsymbol{\omega}_p^T) \quad (21)$$

where $\boldsymbol{\sigma}_p^{\nabla J}$ denotes the Jaumann rate of Cauchy stress, and $\Delta \boldsymbol{\omega}_p$ is the vorticity increment, defined as $\Delta \boldsymbol{\omega}_p = \frac{1}{2} [\nabla \mathbf{v}_p^{n+1} - (\nabla \mathbf{v}_p^{n+1})^\top] \Delta t$. Note that a return mapping algorithm is applied to enforce the Drucker–Prager yield criterion during plastic correction [52, 31] on the Jaumann stress component. The implementation details, including both shear and tensile failure modes, are provided in Appendix A.

3. JAX-MPM: Differentiable meshfree solver for forward and inverse modeling

JAX-MPM is fully implemented within the JAX computational framework [14], a modern backend explicitly designed for differentiable programming and GPU acceleration. This design enables not only high-performance forward particle-based simulations, but also efficient gradient-based optimization for inverse modeling, data assimilation, and seamless integration with machine learning models for hybrid physics–ML workflows.

3.1. Gradient computation by automatic differentiation

To enable efficient gradient-based optimization, JAX-MPM formulates the simulation update rule as a differentiable operator, allowing gradients to propagate through the full trajectory using reverse-mode automatic differentiation.

Let a set $\mathbf{S}^t = \{\mathbf{x}_p^t, \mathbf{v}_p^t, \mathbf{F}_p^t, \rho_p^t\}_{p=1}^{N_p} \in \mathcal{S}$ be a collection of structured simulation states at time step t , where each material point is characterized by its position $\mathbf{x}_p^t \in \mathbb{R}^d$, velocity $\mathbf{v}_p^t \in \mathbb{R}^d$, deformation gradient $\mathbf{F}_p^t \in \mathbb{R}^{d \times d}$, and density $\rho_p^t \in \mathbb{R}$. The space \mathcal{S} denotes the appropriate vector space for these simulation states. We note that additional quantities, such as stress $\boldsymbol{\sigma}_p^t \in \mathbb{R}^{d \times d}$ and equivalent plastic strain $\varepsilon_{eq,p}^t \in \mathbb{R}$, may be included as needed but are omitted here for simplicity.

In the JAX-MPM solver, the evolution of the simulation states \mathbf{S}^t is defined by a recursive mapping:

$$\mathbf{S}^{t+1} = \Phi(\mathbf{S}^t, \boldsymbol{\alpha}) \quad (22)$$

which generates the forward simulation trajectory:

$$\mathbf{S}^1 \xrightarrow{\Phi(\boldsymbol{\alpha})} \mathbf{S}^2 \xrightarrow{\Phi(\boldsymbol{\alpha})} \dots \xrightarrow{\Phi(\boldsymbol{\alpha})} \mathbf{S}^{t+1} \quad (23)$$

Here, the operator $\Phi : \mathcal{S} \times \mathbb{R}^m \rightarrow \mathcal{S}$ denotes the one-step state update procedure of the JAX-MPM solver (see Eqs. (7)–(9)), and $\boldsymbol{\alpha} \in \mathbb{R}^m$ denotes the set of system parameters governing the dynamics. As described in Section 2.2, the update operator Φ is composed of three substeps: particle-to-grid (P2G) transfer Φ_{P2G} , grid-based update Φ_{U} , and grid-to-particle (G2P) projection Φ_{G2P} , such that $\Phi = \Phi_{\text{G2P}} \circ \Phi_{\text{U}} \circ \Phi_{\text{P2G}}$.

Over a complete trajectory with N_t time steps, the ensemble of simulation states $\mathcal{X} = \{\mathbf{S}^t\}_{t=1}^{N_t}$ satisfy the discretized governing equations (3), expressed in compact form as:

$$\mathcal{J}(\mathcal{X}, \boldsymbol{\alpha}) = \mathbf{0}. \quad (24)$$

Within the JAX-MPM framework, the time-stepping operator Φ is *differentiable*, enabling exact and efficient gradient computation with respect to the physical parameters $\boldsymbol{\alpha}$ via reverse-mode automatic differentiation. Consider an arbitrary state variable at time step $(t + 1)$, denoted by $\mathbf{z}^{t+1} \in \mathbf{S}^{t+1}$ (e.g., selecting $\mathbf{z}^{t+1} := \mathbf{v}^{t+1}$). Its derivative with respect to $\boldsymbol{\alpha}$ can be computed recursively through time by applying the chain rule:

$$\frac{d\mathbf{z}^{t+1}}{d\boldsymbol{\alpha}} = \frac{\partial \Phi_{\mathbf{z}}^t}{\partial \mathbf{S}^t} \cdot \frac{d\mathbf{S}^t}{d\boldsymbol{\alpha}} + \frac{\partial \Phi_{\mathbf{z}}^t}{\partial \boldsymbol{\alpha}}, \quad (25)$$

where $\Phi_{\mathbf{z}}^t$ denotes the time-stepping operator at step t , evaluated using input \mathbf{S}^t and restricted to the output \mathbf{z} . In practice, this process continues backward through all prior steps to the initial condition via the recursive mapping in Eq. (22), e.g., $\frac{d\mathbf{S}^t}{d\boldsymbol{\alpha}} = \frac{\partial \Phi^t}{\partial \mathbf{S}^{t-1}} \cdot \frac{d\mathbf{S}^{t-1}}{d\boldsymbol{\alpha}} + \frac{\partial \Phi^t}{\partial \boldsymbol{\alpha}}$. This recursive structure is automatically handled by JAX’s autodiff engine, i.e., $\frac{d\mathbf{z}^{t+1}}{d\boldsymbol{\alpha}} = \text{jax.grad}(\mathbf{z}^{t+1})(\boldsymbol{\alpha})$, which constructs the forward computational graph during execution and traverses it backward to compute gradients.

3.2. PDE-constrained optimization for inverse modeling

Inverse modeling plays a central role in geophysical hazard analysis, where key physical parameters—such as initial velocities or spatially varying friction—cannot be directly observed but significantly influence flow behavior and deposition in events like landslides, dam breaks, and debris flows. To recover such quantities, we formulate the task as a PDE-constrained optimization problem, where the parameters $\boldsymbol{\alpha}$ are inferred by minimizing the discrepancy between simulated and observed data, subject to physical governing equations implemented via JAX-MPM.

To this end, we define a general differentiable output mapping operator \mathcal{Q} that extracts simulated quantities corresponding to observed state data $\mathbf{z}_{l,t}^{\text{obs}} \in \mathbb{R}^d$ at spatial index l and time t . This operator enables the JAX-MPM framework to accommodate both Lagrangian (particle-based) and Eulerian (region-based) forms of supervision. The simulated counterpart at index l is denoted $\mathcal{Q}_l(\mathbf{z}^t)$, where $\mathbf{z}^t \in \mathbf{S}^t$ represents the model state corresponding to the observation.

For Lagrangian supervision, the index l corresponds to a tracked particle, and it simply extracts the quantity associated with l -th particle:

$$\mathcal{Q}_l(\mathbf{z}^t) = [\mathbf{z}^t]_l. \quad (26)$$

For Eulerian supervision, the index l corresponds to a fixed spatial coordinate \mathbf{x}_l , associated with a compact surrounding region $\Omega_l \subset \mathbb{R}^d$ centered at \mathbf{x}_l . In this setting, the simulated quantity is defined as the average over all particles within this region:

$$\mathcal{Q}_l(\mathbf{z}^t) = \frac{1}{|\mathcal{P}_l^t|} \sum_{p \in \mathcal{P}_l^t} \mathbf{z}_p^t, \quad \text{where } \mathcal{P}_l^t = \{p \mid \mathbf{x}_p^t \in \Omega_l\}, \quad (27)$$

where \mathcal{P}_l^t denotes the set of material points located within the Eulerian region Ω_l . This unified formulation provides a consistent interface for extracting outputs for different observational modalities.

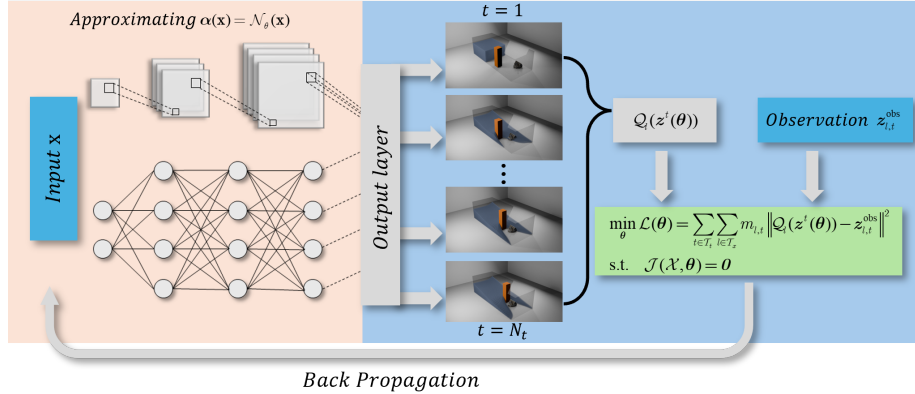


Figure 2: Schematic illustration of the inverse modeling framework in JAX-MPM. A neural network $\mathcal{N}_\theta(\mathbf{x})$ approximates the unknown spatially varying parameter field $\alpha(\mathbf{x})$, which serves as input to the differentiable simulator. The simulation generates state trajectories $\mathbf{z}^t(\theta)$, from which observable quantities $\mathcal{Q}_l(\mathbf{z}^t(\theta))$ are extracted and compared against observed data $\mathbf{z}_{l,t}^{\text{obs}}$. The loss is computed over all space-time points and backpropagated through the entire pipeline via automatic differentiation to update the neural network parameters θ .

The generic inverse problem is depicted in Fig. 2 and can be formulated as:

$$\begin{aligned} \min_{\alpha} \mathcal{L}(\alpha) &= \sum_{t \in \mathcal{T}_t} \sum_{l \in \mathcal{T}_x} m_{l,t} \|\mathcal{Q}_l(\mathbf{z}^t(\alpha)) - \mathbf{z}_{l,t}^{\text{obs}}\|^2, \\ \text{s.t. } \mathcal{J}(\mathcal{X}, \alpha) &= \mathbf{0}. \end{aligned} \quad (28)$$

Here, $\mathbf{z}_{l,t}^{\text{obs}} \in \mathbb{R}^d$ denotes the observed quantity at spatial index l and time t , obtained from measurements or ground-truth data, while \mathbf{z}^t represents the corresponding simulated quantity used for loss evaluation. $\mathcal{T}_t \subseteq \{1, \dots, N_t\}$ is the set of selected observation time steps, and \mathcal{T}_x denotes the set of spatial indices used for supervision. Specifically, the total number of particles is denoted by N_p , and the total number of monitor regions is denoted by N_m . Then, $\mathcal{T}_x \subseteq \{1, \dots, N_p\}$ in the Lagrangian setting and $\mathcal{T}_x \subseteq \{1, \dots, N_m\}$ in the Eulerian setting. The binary mask $m_{l,t} \in \{0, 1\}$ indicates the availability of ground-truth data, and the discretized physical constraints $\mathcal{J}(\mathcal{X}, \boldsymbol{\alpha}) = 0$ are implicitly enforced by the differentiable time-stepping operator Φ , as defined in (22), over the entire simulation trajectory.

In classical adjoint-based PDE-constrained optimization, gradients with respect to $\boldsymbol{\alpha}$ require deriving backward recurrence relations involving the simulation operator Φ . This involves solving an adjoint system backward in time.

In our setting, the total derivative of the loss with respect to $\boldsymbol{\alpha}$ is expressed as:

$$\frac{d\mathcal{L}}{d\boldsymbol{\alpha}} = \sum_{t \in \mathcal{T}_t} \sum_{l \in \mathcal{T}_x} m_{l,t} (\mathcal{Q}_l(\mathbf{z}^t) - \mathbf{z}_{l,t}^{\text{obs}})^\top \cdot \frac{d\mathcal{Q}_l(\mathbf{z}^t)}{d\boldsymbol{\alpha}}, \quad (29)$$

with the sensitivity of outputs governed by the chain rule

$$\frac{d\mathcal{Q}_l(\mathbf{z}^t)}{d\boldsymbol{\alpha}} = \frac{\partial \mathcal{Q}_l}{\partial \mathbf{z}^t} \cdot \frac{\partial \mathbf{z}^t}{d\boldsymbol{\alpha}}, \quad (30)$$

where $\frac{d\mathbf{z}^t}{d\boldsymbol{\alpha}}$ follows the recursive structure as shown in Eq. (25).

Rather than implementing adjoint solvers manually, JAX-MPM leverages reverse-mode automatic differentiation (AD), as detailed in Section 3.1. The entire gradient is computed automatically and efficiently via

$$\frac{d\mathcal{L}}{d\boldsymbol{\alpha}} = \text{jax.grad}(\mathcal{L})(\boldsymbol{\alpha}). \quad (31)$$

This eliminates the need for Jacobian construction or manual derivation of adjoint solvers, making it particularly effective for dynamic inverse problems involving nonlinear physics and complex state trajectories.

Finally, we remark that the parameter field $\boldsymbol{\alpha}$ can take various forms depending on the specific inverse modeling problem. It may represent discrete values specified at particular time steps (e.g., global initial velocity), span the entire simulation trajectory (e.g., basal friction or material constants), or vary continuously in space and/or time (e.g., $\boldsymbol{\alpha} = \boldsymbol{\alpha}(\mathbf{x}, t)$).

When the parameter field is spatially or temporally varying, directly optimizing over high-dimensional fields can be computationally challenging. To address this, we propose to implicitly represent the parameter field using a neural network \mathcal{N}_θ , parameterized by weights $\boldsymbol{\theta} \in \mathbb{R}^{N_\theta}$, as illustrated in Fig. 2. Specifically, given spatial and/or temporal coordinates \mathbf{x} , t , the neural network defines the field as $\boldsymbol{\alpha}(\mathbf{x}, t) = \mathcal{N}_\theta(\mathbf{x}, t)$. This approach enables the learning of a smooth, continuous representation of the parameter field in a flexible and differentiable

manner [41, 32]. In such cases, the inverse problem defined in Eq. (28) does not directly optimize the parameters α , but instead optimizes the neural network weights θ . Regardless of the representation, gradients with respect to either α or θ are computed efficiently and exactly through the automatic differentiation process.

3.3. Software implementation details

The gradient computations described in the previous section rely on differentiating through unrolled simulation trajectories, which can be both computationally intensive and memory-demanding. To support large-scale differentiable simulation, JAX-MPM is implemented on top of the JAX framework, which provides just-in-time (JIT) compilation, automatic differentiation (AD), and GPU acceleration. These capabilities are crucial for achieving high computational efficiency and enabling gradient-based optimization. In the context of inverse modeling of dynamic systems, simulation steps must be executed repeatedly over long time horizons, making both computational speed and memory efficiency critical. To address these demands, JAX-MPM integrates two core strategies: (1) computational acceleration through kernel fusion and loop-level vectorization, and (2) memory optimization via checkpointing and segmented backpropagation. These components are described in the following sections.

3.3.1. Computational speedup using JIT and loop optimization

As summarized in Section 2.2, MPM simulations consist of three core computational stages repeated at each time step: particle-to-grid (P2G) transfer, grid-based updates, and grid-to-particle (G2P) transfer. These operations are inherently parallel over particles and grid nodes, making them ideal targets for optimization. JAX-MPM accelerates these stages using two key strategies: just-in-time (JIT) compilation for kernel fusion and vectorization to parallelize computation across simulation entities.

Remark 2 (JIT Compilation for MPM kernels). Each stage of the MPM update cycle—P2G, grid updates, and G2P—is wrapped using `jax.jit`. This compiles Python functions into efficient XLA-executed code, enabling operation fusion and eliminating Python interpreter overhead.

Remark 3 (Vectorized parallelism). To fully exploit the parallel structure of particle and grid computations, JAX-MPM combines `jax.vmap` and vectorized array operations. Besides using `vmap` for function-level operations such as polar decomposition, we apply batched array operations—e.g., `scatter_add` for momentum transfer in P2G—to update all grid nodes and particles in parallel. This eliminates explicit loops and enables efficient execution on both CPUs and GPUs.

3.3.2. Memory optimization via checkpointing and segmentation

To enable memory-efficient training over long simulation horizons, JAX-MPM incorporates two complementary techniques to reduce memory usage during reverse-mode automatic differentiation: checkpointing of substeps and segmentation of the simulation loop.

Remark 4 (Checkpointing grid operations). Unlike fully Lagrangian methods such as position-based dynamics, MPM adopts a hybrid Eulerian–Lagrangian formulation, where particles interact with a background grid. This incurs high memory costs during backpropagation, as intermediate grid states must be stored. To reduce memory usage, we apply gradient checkpointing: intermediate buffers associated with grid states are discarded during the forward pass and recomputed during the backward pass, retaining only particle-level outputs (e.g., $\mathbf{x}_p^t, \mathbf{v}_p^t$). Similar strategies have been used in prior work [49, 101]. Within the JAX-MPM framework, we implement this using `jax.checkpoint` (also known as `jax.remat`), which re-materializes intermediate computations in `substep` during backpropagation. A representative implementation is shown below:

```
@jax.remat
def substep(carry, _):
    v, x, C, F = carry
    base, fx, w = pre_compute(x)
    F, gv_in, gm_in = p2g(v, x, C, F, base, fx, w)
    gv_out = grid_op(gv_in, gm_in)
    v, x, C = g2p(gv_out, v, x, base, fx, w)
    return (v, x, C, F), None
```

Remark 5 (Segmented simulation loop with `jax.scan`). To reduce memory and compilation overhead, the simulation loop is divided into n segments, each containing N_t/n time steps. Each segment is executed using `jax.scan` and wrapped with `jax.checkpoint`, allowing intermediate values within the segment to be discarded during the forward pass and recomputed during the backward pass. As a result, peak memory usage is determined by the buffer size needed to recompute a single segment, reducing memory complexity from $\mathcal{O}(N_t)$ to $\mathcal{O}(N_t/n)$, where N_t is the total number of time steps. An example implementation is shown below:

```
@jax.remat
def segment(carry):
    return lax.scan(step_fn, carry, None, length=block_size)

for i in range(num_segs):
    carry, _ = segment(carry)
```

4. Numerical results of large scale simulation

This section begins with a validation of JAX-MPM on 2D benchmark problems, followed by large-scale 3D simulations that showcase its effectiveness in modeling complex phenomena such as free-surface flow, rigid-body contact, and granular dynamics, all efficiently accelerated on the GPU.

4.1. Validation of JAX-MPM for 2D cases

4.1.1. Simulation of 2D dam break problem

Accurate simulation of free-surface dynamics is essential for modeling geophysical processes such as floods, dam breaks, and debris surges, where the interaction of inertia, gravity, and evolving boundaries governs flow behavior.

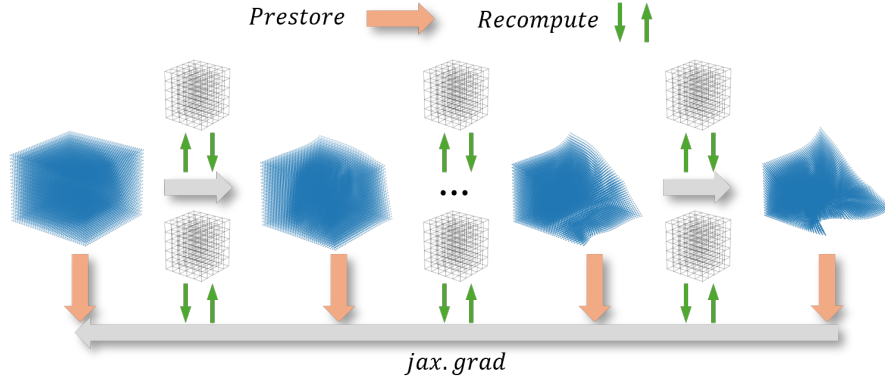


Figure 3: Backward propagation of JAX-MPM with N_t time steps

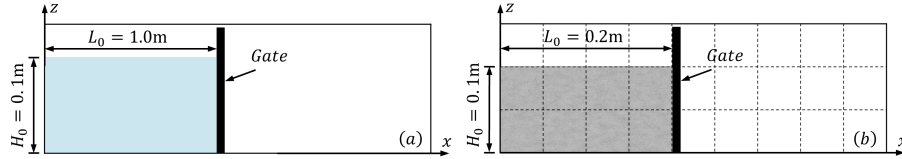


Figure 4: (a): Configuration of 2D shallow dam break; (b): Configuration of quasi-2D granular collapse.

To evaluate the capability of JAX-MPM in capturing such phenomena, we simulate a classical two-dimensional dam break problem under shallow-water assumptions, following the setup in [52]. As illustrated in Fig. 4a, a rectangular column of water with initial height $H_0 = 100$ mm and length $L_0 = 1000$ mm is released at $t = 0$ by removing a gate on the right boundary. The fluid is modeled as a weakly incompressible Newtonian fluid with zero viscosity and friction, allowing direct comparison with analytical results. The simulation domain is discretized with a grid size of $\Delta h = 0.004$ m, and each cell contains 4 particles. The numerical sound speed is $c_n = 35$ m/s and $\Delta t = 1 \times 10^{-5}$ s is set to maintain stability in weakly incompressible flow. Slip boundary conditions are applied to all domain boundaries.

This benchmark admits an analytical solution, providing a rigorous test for validating transient flow front propagation and surface evolution. The horizontal position of the flow front at time t is given by shallow-water theory [89, 52]:

$$x(t) = \left(2\sqrt{H_0|g|} - 3\sqrt{y|g|} \right) t + L_0, \quad (32)$$

where $g = -9.8$ m/s² is gravitational acceleration, and y is the vertical position at the flow front.

We test three different transfer schemes, including FLIP, TPIC, and APIC, within the JAX-MPM framework (see Section 2.2.3). As shown in Fig. 5, all

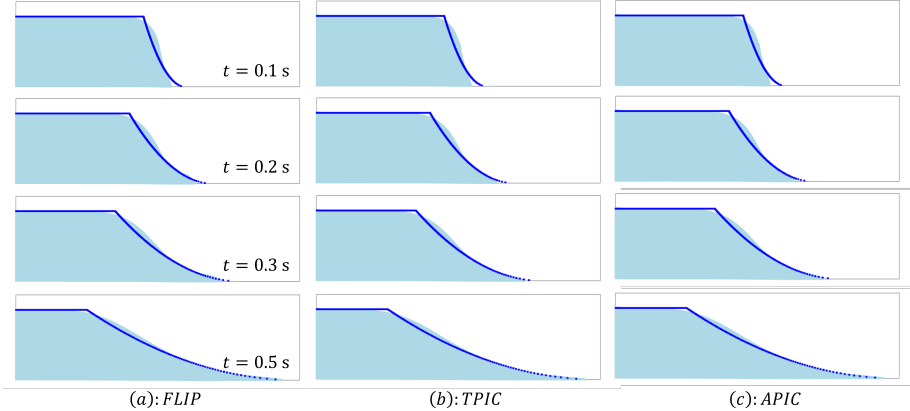


Figure 5: Simulation of 2D shallow dam break problem by JAX-MPM with (a) FLIP, (b) TPIC and (c) APIC.

methods yield results in close agreement with the analytical shallow-water solution overall. Small discrepancies appear during the early stage ($t < 0.3$ s), primarily due to finite-depth effects and vertical accelerations that violate the shallow-water assumptions. As the flow becomes shallower ($t \geq 0.3$ s), the numerical results align more closely with the analytical solution. These observations are consistent with prior findings in [52], confirming the correctness of our implementation.

4.1.2. Simulation of quasi-2D granular collapse: aluminum-bar assemblage

Here, we consider a granular flow benchmark involving the collapse of an aluminum-bar assemblage, following the experimental setup of Bui et al. [15]. The material behavior is governed by the Drucker–Prager elastoplastic model, as described in Sections 2.3 and Appendix A. The material is non-cohesive ($c = 0$ kPa), with density $\rho = 2650$ kg/m³, bulk modulus $K = 0.7$ MPa, Poisson’s ratio $\nu = 0.3$, internal friction angle $\varphi = 19.8^\circ$, and dilatation angle $\psi = 0$.

As shown in Fig. 4b, the initial granular column has dimensions $L_0 = 0.2$ m and $H_0 = 0.1$ m, and is initially confined by a vertical gate. To approximate a quasi-2D condition, the simulation is performed under a plane strain assumption within a computational domain $(x, y, z) \in [0, 600]$ mm \times $[0, 2]$ mm \times $[0, 120]$ mm, discretized into a uniform grid of $300 \times 1 \times 60$ cubic cells. No-slip boundary conditions are applied at the base, while all other boundaries are treated with slip boundary conditions. The simulation employs the FLIP transfer scheme and runs for a total duration of 0.65 s using a fixed time step of $\Delta t = 1 \times 10^{-5}$ s.

Fig. 6a shows the contour plot of the equivalent plastic strain $\varepsilon_{eq,p}$ with peak values concentrated near the base of the aluminum-bar assemblage. These high-strain regions propagate upward, forming a localization pattern consistent with typical shear band development observed in granular collapse scenarios (cf. Fig. 15 in [74]). Fig. 6b presents the predicted free surface and failure surface,

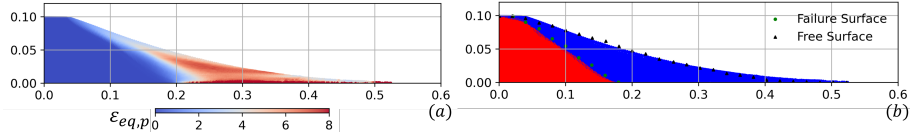


Figure 6: Simulation results of the aluminum-bar assemblage collapse using JAX-MPM. (a) Contour plot of equivalent plastic strain $\varepsilon_{eq,p}$, illustrating shear band development. (b) Comparison with experimental data from Bui et al. [15], where the green dots and black triangles denote the experimentally observed failure surface and free surface, respectively. The simulated failure surface is identified by a threshold $\varepsilon_{eq,p} > 0.03$.

defined by a threshold of $\varepsilon_{eq,p} > 0.03$, both of which show good agreement with experimental observations in [15].

These results demonstrate that the Drucker–Prager model in JAX-MPM accurately captures the key features of granular flow behavior, including shear localization, material failure, and free-surface evolution. Moreover, this benchmark highlights the robustness of the framework in simulating elastoplastic deformation and large-strain dynamics in geomechanical materials.

4.2. Application of JAX-MPM for 3D cases

4.2.1. Simulation of 3D dam break problem

We simulate a three-dimensional (3D) dam break scenario to evaluate the ability of JAX-MPM to capture complex free-surface flow around embedded structures.

As illustrated in Fig. 7, the computational domain is defined as $[0, 1.0] \times [0, 0.5] \times [0, 0.4] \text{ m}^3$. The initial dimensions of the water column are $H_0 = 0.2 \text{ m}$ (height), $L_0 = 0.3 \text{ m}$ (length), and $W_0 = 0.5 \text{ m}$ (width). The fluid is modeled as a weakly compressible Newtonian fluid with a dynamic viscosity of $\mu = 1.01 \times 10^{-3} \text{ Pa} \cdot \text{s}$ and a numerical sound speed of $c_n = 35 \text{ m/s}$. The two rigid square columns, introduced as internal obstacles, have side lengths of 0.04 m and 0.06 m , positioned at $(0.5, 0.3, 0.0) \text{ m}$ and $(0.6, 0.1, 0.0) \text{ m}$, respectively.

A frictionless contact model employing a *predictor–corrector scheme* [10, 47] is used to prevent fluid penetration into the stationary rigid structures. Given the rigidity of these obstacles, enforcing the contact simplifies to eliminating the normal component of the fluid velocity at the fluid-structure interface:

$$\mathbf{v}_I = \tilde{\mathbf{v}}_I - (\tilde{\mathbf{v}}_I \cdot \mathbf{n}_I) \mathbf{n}_I, \quad (33)$$

where $\tilde{\mathbf{v}}_I$ is the predicted fluid velocity vector (*predictor*), \mathbf{v}_I is the corrected velocity vector, and \mathbf{n}_I is the normal vector to the rigid surface. This correction allows slip along the boundaries by preserving the tangential velocity component.

Fig. 8 illustrates the dynamic evolution of the free-surface flow interacting with embedded rigid obstacles. Initially (at $t = 0.12\text{--}0.30 \text{ s}$), the fluid front impacts the columns, causing upward splashing and significant surface deformation. Later stages reveal recirculation zones and lateral flow separation behind the obstacles, clearly demonstrating the framework’s ability to capture complex three-dimensional fluid behaviors induced by rigid boundaries.

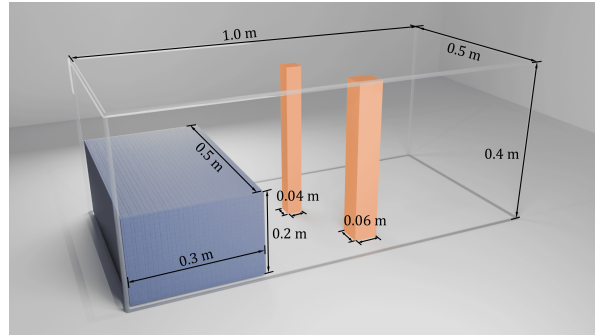


Figure 7: Configuration of 3D dam break simulation with rigid internal obstacles.

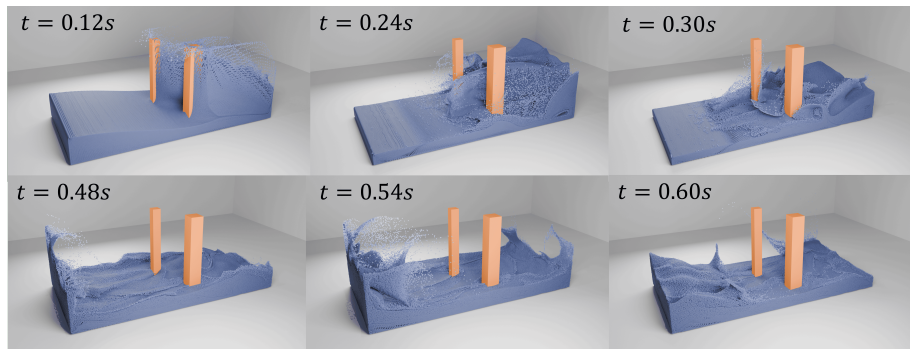


Figure 8: 3D dam break simulation with with rigid internal obstacles.

Besides capturing physically realistic flow dynamics qualitatively, JAX-MPM showcases high computational efficiency. The simulation presented in Fig. 8, featuring over 1.9 million particles and a $200 \times 100 \times 80$ grid, completes 1000 time steps in approximately 8 seconds (see Table 1). This computational performance highlights the scalability of the JAX-based implementation, which benefits from just-in-time (JIT) compilation and GPU acceleration. These features collectively enable fast and stable execution of large-scale geotechnical simulations, positioning JAX-MPM as a powerful computational tool for practical and high-performance modeling.

4.2.2. 3D granular column collapse: Influence of aspect ratio

To evaluate the capability of JAX-MPM in simulating large-scale granular flow behaviors and capturing the influence of geometric factors, we consider a three-dimensional granular column collapse scenario. The primary goal is to investigate how the initial geometry, characterized by different aspect ratios $a = H_0/L_0$ affects the dynamics, runout distance, and failure mechanisms of the granular material. Here, H_0 and L_0 denote the initial height and length of the granular column, respectively. A total of 200,000 time steps are executed,

Table 1: Summary of simulation configurations and computational costs. The label “sim” refers to forward simulations, with runtimes reported for both single precision (float32) and double precision (float64), formatted as “float32 / float64”. The label “sim + grad” denotes inverse simulations involving both forward and gradient computations, performed exclusively in double precision (float64). “Sec/1000 steps” indicates the wall time (in seconds) for every 1000 time steps.

Example	Particle #	Grid resolution	Param #	Sec/1000 steps	Δh
Dam break (Fig. 8)	1,920,000	$200 \times 100 \times 80$	N/A	8.2/35.1 (sim)	1/200
Granular column (Fig. 9)	2,408,448	$400 \times 32 \times 200$	N/A	16.2/69.3 (sim)	1/400
Granular cylinder (Fig. 11)	2,712,960	$400 \times 400 \times 100$	N/A	22.3/98.4 (sim)	1/400
Inv. velocity (Fig. 14)	10,000	150×60	1951	0.62 (sim + grad)	1/100
	40,000	300×120	1951	1.52 (sim + grad)	1/200
Inv. friction (Fig. 15)	6000	200×40	5	0.59 (sim + grad)	1/100

corresponding to 2 s of simulation time with a time step size of $\Delta t = 10^{-5}$ s. The material parameters remain the same as in Section 4.1.2.

In this test, we select four aspect ratios for systematic comparison: $a = 0.5, 1.0, 2.0,$ and 3.0 . As shown in Fig. 9, higher aspect ratios result in a larger portion of the granular column experiencing free fall, thereby decreasing the size of the static basal region and increasing lateral spreading. The final runout distance L_f is measured and normalized by the initial base length L_0 , defined as $d_n = (L_f - L_0)/L_0$. The normalized runout distance increases from approximately 2.05 at $a = 0.5$ to 3.97 at $a = 1.0$, 7.76 at $a = 2.0$, and 10.65 at $a = 3.0$. While runout increases with the aspect ratio, the growth rate diminishes at higher values, reflecting a transition from linear to sublinear scaling. This trend is consistent with experimental observations reported in [87], where the normalized runout distance scales approximately as $d_n \propto a$ for small a and $d_n \propto a^{0.7}$ for larger a .

Computational scalability

To evaluate the computational performance of JAX-MPM, we benchmark the 3D granular column collapse simulation against the open source C++ solver CB-Geo [60]. Simulations are performed at five resolutions, with grid spacings ranging from $\Delta h = 0.015$ to $\Delta h = 0.004$, corresponding to particle counts from approximately 1.7×10^4 to 9.0×10^5 . Wall-clock times are measured for every 1000 simulation steps across the following computational configurations: (1) CB-Geo on multiple CPUs and (2) JAX-MPM on GPU. CPU benchmarks are conducted on an AMD EPYC 7763 processor with 128 threads, whereas GPU benchmarks utilize an NVIDIA A100 accelerator.

It should be noted that CB-Geo employs a Mohr–Coulomb material model, as the built-in solver does not currently support Drucker–Prager plasticity. Although Mohr–Coulomb models are generally more computationally demanding due to their nonsmooth yield surfaces, their computational complexity remains comparable to that of Drucker–Prager models. Therefore, the presented benchmarking results still provide valuable insight into the relative computational scalability and efficiency of both solvers on CPU and GPU platforms.

As shown in Fig. 10, JAX-MPM executed on GPU substantially outperforms CB-Geo on CPU configurations across all tested resolutions, exhibiting the

most favorable scaling behavior. At the highest resolution ($\Delta h = 0.004$, 900,000 particles), GPU-accelerated JAX-MPM completes 1000 steps in roughly 9 seconds, representing a speedup more than $7\times$ compared to CB-Geo running on CPU.

The strong GPU performance and scaling are enabled by JAX-MPM’s effective utilization of GPU acceleration, just-in-time (JIT) compilation, and fused kernel execution (see Section 3.3.1). These features significantly enhance the solver’s capability for moderate to large-scale geomechanical problems, highlighting the computational advantages of differentiable simulation frameworks built on modern array-programming infrastructures.

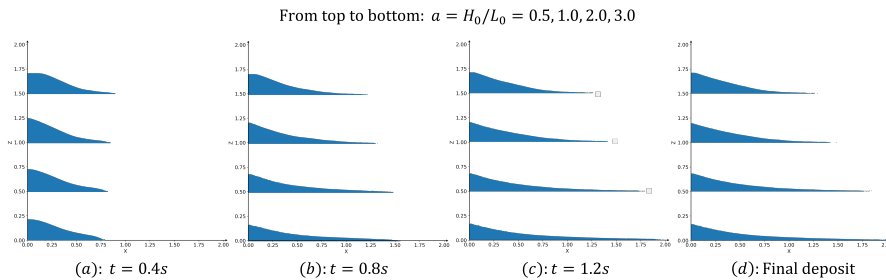


Figure 9: 3D granular column collapse with varying aspect ratios. 2D deposit profiles are shown at $t = 0.4$ s, 0.8 s, 1.2 s, and final deposit for initial aspect ratios $a = H_0/L_0 = 0.5, 1.0, 2.0, 3.0$. Higher aspect ratios lead to greater vertical collapse and longer runout distances due to enhanced free-fall and mass mobilization.

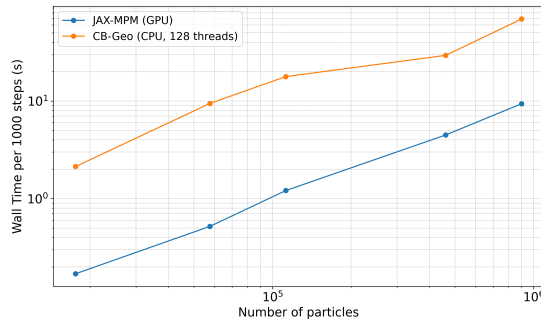


Figure 10: Computational scaling (wall-clock time) comparison between JAX-MPM (GPU) and the open-source C++ solver CB-Geo (CPU) [60] across five simulation resolutions (from approximately 17.6k to 900k particles). All simulations are performed in double precision (float64).

4.2.3. 3D granular cylinder collapse: Influence of friction angle

In this example, we investigate the collapse of a 3D granular cylinder with varying internal friction angles $\varphi = 20^\circ, 25^\circ, 35^\circ$, and 40° . The simulation runs for 1 s using a time step size of $\Delta t = 1 \times 10^{-5}$ s, totaling 100,000 time steps. The Drucker–Prager elastoplastic constitutive model is employed, with



Figure 11: 3D granular cylinder collapse with varying friction angles. Final deposit profiles for friction angles $\varphi = 20^\circ, 25^\circ, 35^\circ, 40^\circ$. Higher friction results in steeper, more confined piles and reduced spreading due to increased shear resistance.

all other material parameters remaining identical to those detailed in Section 4.1.2. Friction significantly influences shear resistance, flow mobility, and the final deposit geometry in granular flows.

As shown in Fig. 11, increasing the friction angle results in steeper and more confined final deposits with shorter runouts, reflecting increased resistance to shear deformation. These results align well with theoretical predictions and prior experimental observations reported in the literature [59, 57].

The JAX-MPM simulation involves over 2.7 million particles on a $400 \times 400 \times 100$ computational grid (approximately 16 million grid nodes) and completes every 1000 simulation steps in approximately 22 seconds (single precision) and 98 seconds (double precision) using a single NVIDIA A100 GPU. For comparison, a recent high-performance Fortran-based MPM solver employing dynamic load balancing (DLB) reported a runtime of 688 seconds for a similar scenario, involving roughly the same number of particles and comparable material models, with a grid resolution of $280 \times 280 \times 120$ (approximately 9.4 million grid nodes), executed on 288 CPU cores [45]. Without DLB, the runtime increases significantly to approximately 13,803 seconds. Relative to the Fortran implementation with DLB, JAX-MPM achieves roughly a $7\times$ speedup, and nearly $140\times$ over the baseline version without DLB. These benchmarks underscore the exceptional computational efficiency and scalability of the JAX-MPM framework, particularly when leveraging modern GPU acceleration for large-scale geomechanical simulations.

5. Inverse modeling of geophysical flows using JAX-MPM

Inverse modeling plays a critical role in geophysical flow analysis, enabling the recovery of unobservable system parameters and guiding the design of effective mitigation strategies. Parameters such as initial velocity fields and spatially varying basal friction fundamentally influence flow dynamics, runout extent, and energy dissipation, yet they are often difficult or impossible to measure directly. In such cases, inverse modeling provides a powerful tool for post-event analysis, model calibration, and data-driven control.

Prior studies have approached inverse problems in geomechanics using techniques ranging from traditional back-analysis [17], Bayesian inference with surrogate models [103], to more recent differentiable simulators [21, 22]. These

developments reflect a growing trend toward leveraging gradient-based optimization and automatic differentiation for efficient parameter inference and process learning [35, 84].

In this section, we further evaluate the JAX-MPM framework’s capability for learning-based inverse modeling through a series of parameter estimation tasks that are difficult to address with traditional non-differentiable solvers. Specifically, we consider two representative inverse problems in a dam-break setting: recovering unknown initial velocity fields (Sections 5.1–5.2) and estimating spatially variable friction coefficients (Section 5.3) from sparse dynamic measurements.

Unless otherwise specified, all inverse modeling experiments in this section are optimized using the Adam algorithm with a decaying learning rate starting at $lr = 0.1$.

5.1. Inverse prediction of initial velocity constant

We begin by testing the inverse estimation of a scalar parameter that defines the initial horizontal velocity field in a 2D dam-break scenario (see Section 4.1.1). In this case study, the ground-truth initial velocity is prescribed as $v_x^0 = \bar{\alpha}(H_0 - y)$ with $\bar{\alpha} = 2.0$ and $v_y^0 = 0$, where $\bar{\alpha}$ is the unknown parameter to be inferred. The reference simulation assumes an inviscid fluid ($\mu = 0$) with a sound speed of $c_0 = 50$ m/s. Both the height and length of the initial water column are $H_0 = L_0 = 0.5$ m. The computational domain is discretized using a grid spacing of $\Delta h = 0.01$ m, with four particles per cell. The simulation is run over a duration of $t = 0.3$ s with a time step of $\Delta t = 3 \times 10^{-5}$ s.

The inverse problem is formulated via a PDE-constrained optimization (28), aiming to recover the unknown parameter α by minimizing the loss computed from the discrepancy between simulated dynamics and reference observation data. The objective is evaluated over the final $|\mathcal{T}_t| = 100$ frames (i.e., the last 0.03 s) sampled from the final 1000 simulation time steps. We consider three observation strategies, each defined by a specific choice of the simulation variable \mathbf{z}^t and spatial indices \mathcal{T}_x :

(1) Full particle position supervision (Lagrangian): All material points are tracked, with the simulation variable set to particle positions, i.e., $\mathbf{z}^t = \mathbf{x}^t$. Therefore, the observed quantity is defined as $\mathcal{Q}_l(\mathbf{z}^t) = \mathbf{x}_l^t$ for each index $l \in \mathcal{T}_x$, where $|\mathcal{T}_x| = 10,000$.

(2) Sparse particle position supervision (Lagrangian): A randomly selected subset of particles is observed, with $|\mathcal{T}_x| = 100$. The simulation variable remains $\mathbf{z}^t = \mathbf{x}^t$, and the mapping $\mathcal{Q}_l(\mathbf{z}^t) = \mathbf{x}_l^t$ is applied identically.

(3) Sparse velocity-monitor supervision (Eulerian): Predefined spatial regions are used to monitor average particle velocities. The simulation variable is set to particle velocities, $\mathbf{z}^t = \mathbf{v}^t$, and the observed simulated quantity is computed as:

$$\mathcal{Q}_l(\mathbf{z}^t) = \frac{1}{|\mathcal{P}_l^t|} \sum_{p \in \mathcal{P}_l^t} \mathbf{v}_p^t, \quad (34)$$

where $\mathcal{P}_l^t = \{p \mid \mathbf{x}_p^t \in \Omega_l\}$ denotes the set of particles located within the l -th Eulerian monitor region Ω_l . Each Ω_l is defined as a square region with half-size 0.01 m. Here, as shown in Fig. 12, we consider $N_m = 9$ monitor regions, whose centers are placed on the 3×3 grids located at $\{0.2, 0.3, 0.4\} \times \{0.1, 0.2, 0.3\}$.

Optimization starts from an initial guess $\alpha_0 = 0.1$. Fig. 12(a-b) present the training loss and the evolution of the recovered parameter α^h , respectively. Among the three strategies, velocity supervision achieves the fastest and most stable convergence, despite using the fewest observations. This reflects better alignment between the inferred parameter and the supervised quantity, as α directly influences the velocity field. Interestingly, the sparse particle supervision achieves comparable or even faster convergence than the full-particle case. While the full-field data provides dense information, it also introduces more variability in the gradient signal, which may lead to oscillations during training.

All methods ultimately recover α to values close to the ground truth ($\alpha = 2.0$). Fig. 13 visualizes the flow fields at $t = 0.15$ s and $t = 0.30$ s for the initial guess, the ground truth, and the result obtained using the velocity monitor-based (Eulerian) supervision. The final deposit shape closely matches the reference simulation, indicating that the inferred parameter leads to physically accurate flow dynamics. These results confirm the effectiveness of JAX-MPM in solving inverse problems using both Lagrangian and Eulerian observation types within a unified, fully differentiable framework.

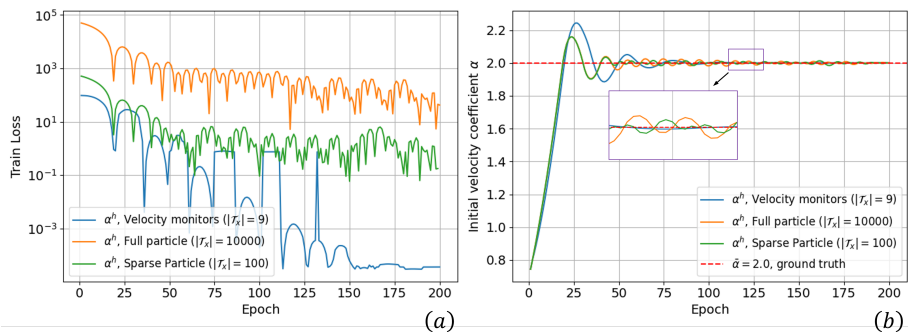


Figure 12: Training evolution for inverse recovery of the initial velocity constant α under three supervision strategies. (a): training loss over epochs. (b): evolution of the estimated parameter α^h .

5.2. Inverse prediction of initial velocity field

In this example, we adopt the same simulation setup as in the previous experiment (Section 5.1), but consider a more general scenario in which the initial horizontal velocity varies spatially and cannot be described by a single parameter. Specifically, the reference velocity is defined as:

$$v_x^0 = 2.0 \left(1 - \left(\frac{y}{H_0} \right)^2 \right) + 0.2 \sin \left(4\pi \frac{y}{H_0} \right),$$

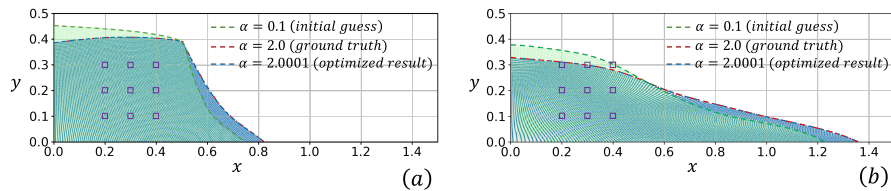


Figure 13: Comparison of flow geometries at (a) $t = 0.15$ s and (b) $t = 0.30$ s for the initial guess, ground truth, and optimized initial velocity, obtained by using the velocity monitor-based (Eulerian) supervision. The final deposit shape produced by JAX-MPM closely matches the reference solution, confirming the accuracy of scalar parameter recovery. Purple squares indicate the locations of the $N_m = 9$ velocity monitors, arranged in a 3×3 grid at coordinates $\{0.2, 0.3, 0.4\} \times \{0.1, 0.2, 0.3\}$.

which combines a parabolic base profile with a high frequency sine perturbation.

Our objective is to recover the continuous initial velocity field $v_x^0(y)$ from observational data. To this end, we parameterize the velocity profile using a neural network \mathcal{N}_θ , where θ denotes the trainable weights, and learn a mapping from the vertical coordinate y to the initial velocity v_x^0 . Since the goal is to reconstruct a continuous spatial velocity field, velocity monitor data is not employed in this experiment. Instead, we use sparse-particle (Lagrangian) supervision scheme introduced in Section 5.1. To assess the effect of observation sparsity, we randomly select subsets of particles at three sampling densities: 100, 500, and 1000 particles ($|\mathcal{T}_x| \in \{100, 500, 1000\}$). These sampled particle trajectories form the observation dataset. In all cases, the loss is evaluated over the final $|\mathcal{T}_t| = 100$ frames (last 0.03s) sampled from the last 1000 time steps, consistent with the previous experiment. We use a feedforward neural network comprising three hidden layers with 30 ReLU-activated neurons each.

As shown in Fig. 14(a–b), the training loss for $|\mathcal{T}_x| = 500$ and $|\mathcal{T}_x| = 1000$ decreases steadily and converges after around 400 epochs. In contrast, the loss for $|\mathcal{T}_x| = 100$ remains nearly flat throughout training, indicating that the data is too sparse to drive meaningful parameter updates. The final relative L_2 errors between predicted and reference velocity fields are 45.1% for 100 particles, 6.4% for 500, and 3.7% for 1000. These results suggest the presence of an observation sufficiency threshold for effective field reconstruction in this setting: the $|\mathcal{T}_x| = 100$ case fails to provide adequate information for learning, while increasing the number of observations to 500 and 1000 significantly improves accuracy.

Fig. 14c presents the reconstructed initial velocity profiles against the ground truth. Both the $|\mathcal{T}_x| = 500$ and $|\mathcal{T}_x| = 1000$ cases successfully capture the overall profile, particularly in the upper region. The $|\mathcal{T}_x| = 1000$ result provides a smoother and more accurate reconstruction, while the $|\mathcal{T}_x| = 500$ case slightly underestimates local variations, due to limited spatial coverage, which constrains the model’s ability to resolve finer features. The deviations near the lower boundary highlight a common challenge in inverse field recovery. This region is influenced by upstream particle motion, making it harder to attribute observed

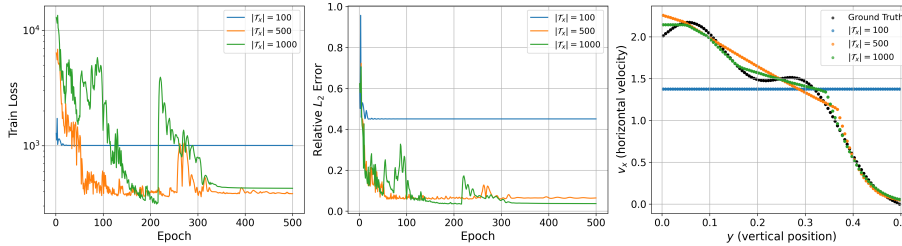


Figure 14: Inverse recovery of a spatially varying initial velocity field using a neural network. (a) Training loss over epoch, (b) convergence of relative error, and (c) comparison between the learned and reference velocity profiles.

behavior to local initial conditions. Additionally, boundary particles often slow down or stop early due to contact, contributing less to the loss. Together, these factors weaken gradient signals and reduce reconstruction accuracy near the bottom of the domain. In contrast, the $|\mathcal{T}_x| = 100$ case fails to recover any meaningful spatial structure, resulting in a nearly constant prediction. This highlights again a lower limit on observation density below which continuous field reconstruction becomes ill-posed or ineffective.

These results demonstrate the effectiveness of JAX-MPM for learning spatially varying fields with neural networks. JAX-MPM enables accurate reconstruction of complex initial and boundary conditions via gradient-based optimization, making it a versatile tool for data-driven hazard analysis, model calibration, and predictive simulation.

5.3. Inverse prediction of frictional coefficient

Frictional heterogeneity is common in real-world geohazards, and it strongly influences flow mobility, energy dissipation, and deposition patterns. However, frictional properties are rarely measurable in situ, necessitating inverse modeling to recover them from observable outcomes.

In this example, we demonstrate the ability of JAX-MPM to recover spatially varying Coulomb friction coefficients μ_f along the bottom boundary of a 2D dam-break scenario, using particle trajectory observations. The system is initialized in a standard dam-break configuration within a domain of $L = 1.6$ m (length) and $H = 0.4$ m (height), with an initial water column of $L_0 = 0.5$ m and $H_0 = 0.3$ m. The bottom surface is divided into four equal-length segments, each assigned a ground-truth friction coefficient $\mu_f = [0.0, 0.5, 0.1, 0.2]$, which are treated as trainable parameters during optimization. Since different segments interact with the flow at different stages, supervision is provided using particle trajectories sampled from $|\mathcal{T}_t| = 1000$ observation frames, evenly spaced throughout the full 10,000-step simulation (corresponding to 0.4 s with a time step size of $\Delta t = 4 \times 10^{-5}$ s). Two observation densities are tested: $|\mathcal{T}_x| = 100$ and $|\mathcal{T}_x| = 500$ randomly selected particles.

Frictional contact is modeled using the Coulomb friction law proposed by Bardenhagen et al. [6], which modifies the tangential velocity at contact nodes

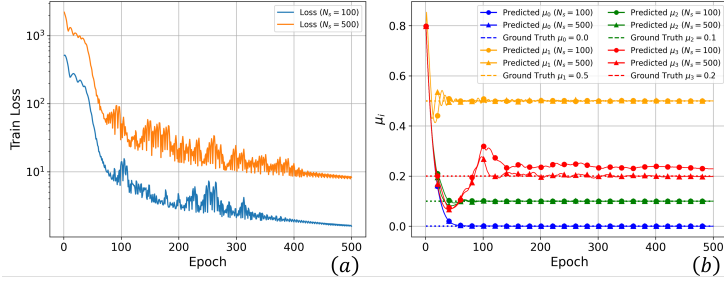


Figure 15: Inverse recovery of spatially varying Coulomb friction coefficients in a segmented dam-break domain. (a) Training loss over epoch, (b) Evolution of the predicted friction coefficients μ_f for each segment compared to the ground truth values.

based on particle-wall interaction. The corrected grid velocity \mathbf{v}_i^{n+1} at contact node i is given by:

$$\mathbf{v}_i^{n+1} = \tilde{\mathbf{v}}_i^{n+1} - [\Delta \mathbf{v} \cdot \mathbf{n}_i] (\mathbf{n}_i + \mu' \mathbf{n}_i \times \boldsymbol{\omega}), \quad (35)$$

where:

$$\Delta \mathbf{v} := \tilde{\mathbf{v}}_I^{n+1}, \quad \boldsymbol{\omega} = \frac{\Delta \mathbf{v} \times \mathbf{n}_I}{\|\Delta \mathbf{v} \times \mathbf{n}_I\|}, \quad \mu' = \min \left[\mu, \frac{\|\Delta \mathbf{v} \times \mathbf{n}_I\|}{\Delta \mathbf{v} \cdot \mathbf{n}_I} \right] \quad (36)$$

where $\tilde{\mathbf{v}}_i^{n+1}$ is the intermediate grid velocity before applying contact corrections, and \mathbf{n}_i is the normal vector at the contact surface (e.g., $[0, -1]$ for bottom wall contact).

As shown in Fig. 15, both the $|\mathcal{T}_x| = 100$ and $|\mathcal{T}_x| = 500$ cases recover the first three upstream friction segments (μ_0, μ_1, μ_2) with high accuracy, closely matching their ground-truth values. The key difference appears in the downstream segment μ_3 , where the estimate from $|\mathcal{T}_x| = 100$ converges to 0.229, corresponding to a 14.5% relative error, while the $|\mathcal{T}_x| = 500$ case yields a much closer value of 0.198, with only a 1.0% error. This comparison highlights the role of observation density in improving parameter accuracy, particularly for regions that interact with the flow later in time. Additionally, we observe faster convergence on the upstream segments. This reflects the cumulative nature of frictional effects: parameters that influence the flow earlier affect a larger number of particle trajectories and thus produce stronger gradient signals. In contrast, the downstream segments interact with the flow later and more locally, making them harder to recover accurately, especially under sparse supervision.

This example demonstrates that JAX-MPM can accurately recover spatially varying friction coefficients from partial trajectory data, even in contact-dominated systems with discontinuous boundary conditions. Its differentiable Lagrangian formulation enables direct optimization of localized, non-smooth parameters from sparse observations. This capability is essential for real-world geomechanical applications, where frictional heterogeneity is common and observational data is often limited.

6. Conclusion

We presented JAX-MPM, a fully differentiable, GPU-accelerated Material Point Method (MPM) framework tailored for large-deformation simulation and inverse modeling in geomechanics and solid mechanics. Built entirely on the JAX ecosystem, the framework leverages modern differentiable programming capabilities, including automatic differentiation, just-in-time (JIT) compilation, and vectorized GPU execution, to support scalable, end-to-end optimization pipelines. JAX-MPM integrates naturally with neural network libraries, enabling hybrid physical–ML workflows for data-driven modeling and field reconstruction.

The framework employs a unified inverse modeling approach that accommodates both particle-based and region-based observations, allowing flexible inference of physical parameters from diverse data sources. We validated JAX-MPM on a suite of forward benchmarks, including dam-break problems and granular collapses in both 2D and 3D, demonstrating its accuracy, efficiency, and scalability. Compared to traditional CPU-based implementations in C++ or Fortran, JAX-MPM achieves significant speedups through GPU acceleration, while providing native support for gradient-based optimization and machine learning integration. To evaluate inverse modeling performance, we conducted several tasks such as initial condition reconstruction and spatially varying friction estimation. These results position JAX-MPM as a robust and extensible platform for differentiable simulation in geomechanics.

Looking ahead, several opportunities remain for further development. First, while checkpointing helps mitigate memory usage during training, the backward pass in high-resolution simulations remains demanding—particularly with small time steps or dense grids. Enhancing memory management and gradient computation efficiency will be key to scaling up optimization. Second, modeling non-smooth or highly nonlinear materials—such as Drucker–Prager plasticity—can cause instability or undefined gradients during automatic differentiation. Addressing this may require customized backward kernels or hybrid constitutive models that blend physics-based laws with neural approximators. Lastly, extending the framework to support implicit time integration could improve numerical stability and enable longer simulation horizons. While feed-forward neural networks are currently used in JAX-MPM to approximate unknown parameter fields, the framework’s general differentiability also allows for alternative approaches such as symbolic regression or hybrid formulations (e.g., NIM [33], enrichment functions incorporating prior knowledge).

Overall, JAX-MPM advances differentiable physics in continuum mechanics by bridging high-fidelity simulation with scalable gradient-based optimization. It offers a flexible and efficient foundation for future research in inverse modeling, hybrid physical–ML systems, and learning-enabled digital twins for geohazard analysis.

Appendix A. Stress update for Drucker–Prager elastoplasticity

This appendix details the implementation of Drucker–Prager constitutive model. The model parameters are defined as

$$q_\varphi = \frac{6 \sin \varphi}{\sqrt{3}(3 + \sin \varphi)}, \quad k_\varphi = \frac{6c \cos \varphi}{\sqrt{3}(3 + \sin \varphi)}, \quad q_\psi = \frac{6 \sin \psi}{\sqrt{3}(3 + \sin \psi)},$$

where φ and ψ are the internal friction and dilation angles, respectively, and c is the cohesion. The model also uses the elastic shear and bulk moduli G and K .

The constitutive model follows a rate-independent, return-mapping algorithm with Drucker–Prager-type shear and tensile yielding. The Jaumann stress rate ensures objectivity under large deformation. The procedure is as follows:

- (1) *Elastic trial stress.* For clarity, we reformulate the stress tensor in Eq. (21) using index notation. The trial stress at t^{n+1} is evaluated by combining the rotated stress and the deformation increment:

$${}^* \sigma_{ij}^{n+1} = \sigma_{ij}^{Rn} + C_{ijkl} \Delta d_{kl} \quad (\text{A.1})$$

where C_{ijkl} is the tangential stiffness tensor of the material, σ_{ij}^{Rn} accounts for material rotation via the Jaumann rate:

$$\sigma_{ij}^{Rn} = \sigma_{ij}^n + \sigma_{ik}^n \Delta \omega_{jk} + \sigma_{jk}^n \Delta \omega_{ik} \quad (\text{A.2})$$

- (2) *Compute trial invariants.* The spherical (mean) and effective shear stresses of the trial stress are given by:

$${}^* \sigma_m^{n+1} = \frac{1}{3} {}^* \sigma_{kk}^{n+1} \quad (\text{A.3})$$

$${}^* \tau^{n+1} = \sqrt{\frac{1}{2} {}^* s_{ij}^{n+1} {}^* s_{ij}^{n+1}} \quad (\text{A.4})$$

where ${}^* s_{ij} = {}^* \sigma_{ij}^{n+1} - {}^* \sigma_m^{n+1}$ is the deviatoric components of trial stress.

- (3) *Evaluate yield conditions.* Plastic yielding is governed by three criteria:

$$f^s = {}^* \tau^{n+1} - k_\varphi + q_\varphi {}^* \sigma_m^{n+1} \quad (\text{A.5})$$

$$f^t = {}^* \sigma_m^{n+1} - \sigma^t \quad (\text{A.6})$$

$$h = {}^* \tau^{n+1} - \tau^P - \alpha^P ({}^* \sigma_m^{n+1} - \sigma^t) \quad (\text{A.7})$$

where f^s is the Drucker–Prager shear yield function, and f^t represents a tensile cutoff. And h [102] is a auxiliary function with the constants τ^P and α^P given by:

$$\tau^P = k_\varphi - q_\varphi \sigma^t \quad \text{and} \quad \alpha^P = \sqrt{1 + q_\varphi^2} - q_\varphi \quad (\text{A.8})$$

The trial stress state is classified into the following three zones:

(a) Zone I (Elastic region):

$$f^s(*\sigma_m^{n+1}, *\tau^{n+1}) \leq 0 \quad \text{and} \quad f^t(*\sigma_m^{n+1}) < 0 \quad (\text{A.9})$$

No yielding occurs, and the trial stress is accepted without correction.

(b) Zone II (Shear failure region):

$$\text{Either} \quad \begin{cases} f^s(*\sigma_m^{n+1}, *\tau^{n+1}) > 0 & \text{and} & f^t(*\sigma_m^{n+1}) < 0 \\ h(*\sigma_m^{n+1}, *\tau^{n+1}) > 0 & \text{and} & f^t(*\sigma_m^{n+1}) \geq 0 \end{cases} \quad (\text{A.10})$$

(c) Zone III (Tensile failure region):

$$h(*\sigma_m^{n+1}, *\tau^{n+1}) \leq 0 \quad \text{and} \quad f^t(*\sigma_m^{n+1}) \geq 0 \quad (\text{A.11})$$

(4) *Shear failure correction (Zone II).*

In Zone II, the stress is returned to the shear yield surface $f^s = 0$ by a radial return rule, assuming incompressible plastic flow. The updated stress components are:

$$\sigma_m^{n+1} = *\sigma_m^{n+1} - Kq_\psi \Delta\lambda^s \quad (\text{A.12})$$

$$\tau^{n+1} = k_\varphi - q_\varphi \sigma_m^{n+1} \quad (\text{A.13})$$

$$\sigma_{ij}^{n+1} = \frac{\tau^{n+1}}{*\tau^{n+1}} *s_{ij}^{n+1} + \sigma_m^{n+1} \delta_{ij} \quad (\text{A.14})$$

and the equivalent plastic strain increment is:

$$\Delta\varepsilon_{eq,p} = \Delta\lambda^s \sqrt{\frac{1}{3} + \frac{2}{9}q_\psi^2} \quad (\text{A.15})$$

The proportionality constant $\Delta\lambda^s$ is obtained by enforcing consistency with the yield surface:

$$\Delta\lambda^s = \frac{f^s}{G + Kq_\varphi q_\psi} \quad (\text{A.16})$$

(5) *Tensile failure correction (Zone III).*

In Zone III, tensile failure occurs when the trial mean stress exceeds σ^t and the state lies outside the transition surface. The material can no longer sustain tension, and the stress is corrected to cap the mean stress at σ^t .

The corrected stress and equivalent plastic strain are computed as:

$$\sigma_{ij}^{n+1} = *\sigma_{ij}^{n+1} + (\sigma^t - *\sigma_m^{n+1}) \delta_{ij} \quad (\text{A.17})$$

$$\Delta\varepsilon_{eq,p} = \frac{\sqrt{2}}{3} \Delta\lambda^t \quad (\text{A.18})$$

The proportionality constant $\Delta\lambda^t$ is derived from the consistency condition $f^t = 0$:

$$\Delta\lambda^t = \frac{*\sigma_m^{n+1} - \sigma^t}{K} \quad (\text{A.19})$$

Appendix B. Velocity transfer scheme

JAX-MPM supports multiple grid-to-particle (G2P) transfer schemes, including PIC, FLIP, APIC, and TPIC. Among them, APIC [55] and TPIC [71] retain the same velocity update formulation as PIC for computing the particle velocity \mathbf{v}_p^n , but additionally incorporate particle-level information such as affine velocity fields or velocity gradients to reduce numerical dissipation and enhance stability. These additional particle quantities—such as the affine matrix \mathbf{B}_p^n in APIC or the velocity gradient $\nabla \mathbf{v}_p^n$ in TPIC—are evaluated during the G2P step and reused in the subsequent P2G step to compute the nodal velocity field.

In APIC, the nodal velocity at time step n is given by:

$$\mathbf{v}_i^n = \frac{1}{m_i^n} \sum_p \phi_{ip}^n m_p \left(\mathbf{v}_p^n + \mathbf{B}_p^n \cdot (\mathbf{D}_p^n)^{-1} \cdot (\mathbf{x}_i^n - \mathbf{x}_p^n) \right) \quad (\text{B.1})$$

where $\mathbf{B}_p^n = \sum_i \phi_{ip}^{n-1} \mathbf{v}_i^n \otimes (\mathbf{x}_i^{n-1} - \mathbf{x}_p^{n-1})$, and $\mathbf{D}_p^n = \sum_i \phi_{ip}^n (\mathbf{x}_i^n - \mathbf{x}_p^n) \otimes (\mathbf{x}_i^n - \mathbf{x}_p^n)$ is the moment matrix.

In TPIC, the affine contribution is replaced by a particle velocity gradient $\nabla \mathbf{v}_p^n$, which is derived from prior particle and grid states. The nodal velocity is then computed as:

$$\mathbf{v}_i^n = \frac{1}{m_i^n} \sum_p \phi_{ip}^n m_p \left(\mathbf{v}_p^n + \nabla \mathbf{v}_p^n \cdot (\mathbf{x}_i^n - \mathbf{x}_p^n) \right) \quad (\text{B.2})$$

References

- [1] Abraham, M.T., Satyam, N., Reddy, S.K.P., Pradhan, B., 2021. Runout modeling and calibration of friction parameters of kurichermala debris flow, india. *Landslides* 18, 737–754.
- [2] Allen, K., Lopez-Guevara, T., Stachenfeld, K.L., Sanchez Gonzalez, A., Battaglia, P., Hamrick, J.B., Pfaff, T., 2022. Inverse design for fluid-structure interactions using graph network simulators. *Advances in Neural Information Processing Systems* 35, 13759–13774.
- [3] Andersen, S., Andersen, L., 2010. Modelling of landslides with the material-point method. *Computational Geosciences* 14, 137–147.
- [4] Augarde, C.E., Lee, S.J., Loukidis, D., 2021. Numerical modelling of large deformation problems in geotechnical engineering: A state-of-the-art review. *Soils and Foundations* 61, 1718–1735.
- [5] Bandara, S., Soga, K., 2015. Coupling of soil deformation and pore fluid flow using material point method. *Computers and geotechnics* 63, 199–214.
- [6] Bardenhagen, S., 2001. An improved contact algorithm for the material point method and application to stress propagation in granular material. *Comput Model Eng Sci* 2, 509.
- [7] Bardenhagen, S., 2002. Energy conservation error in the material point method for solid mechanics. *Journal of Computational Physics* 180, 383–403.
- [8] Bardenhagen, S., Brackbill, J., Sulsky, D., 2000. The material-point method for granular materials. *Computer methods in applied mechanics and engineering* 187, 529–541.
- [9] Baydin, A.G., Pearlmutter, B.A., Radul, A.A., Siskind, J.M., 2018. Automatic differentiation in machine learning: a survey. *Journal of Machine Learning Research* 18, 1–43.
- [10] Belytschko, T., Neal, M.O., 1991. Contact-impact by the pinball algorithm with penalty and lagrangian methods. *International journal for numerical methods in engineering* 31, 547–572.
- [11] Bezgin, D.A., Buhendwa, A.B., Adams, N.A., 2023. Jax-fluids: A fully-differentiable high-order computational fluid dynamics solver for compressible two-phase flows. *Computer Physics Communications* 282, 108527.
- [12] Blondel, M., Roulet, V., 2024. The elements of differentiable programming. *arXiv preprint arXiv:2403.14606* .
- [13] Brackbill, J.U., Ruppel, H.M., 1986. Flip: A method for adaptively zoned, particle-in-cell calculations of fluid flows in two dimensions. *Journal of Computational physics* 65, 314–343.

- [14] Bradbury, J., Frostig, R., Hawkins, P., Johnson, M.J., Leary, C., Maclaurin, D., Necula, G., Paszke, A., VanderPlas, J., Wanderman-Milne, S., Zhang, Q., 2018. JAX: composable transformations of Python+NumPy programs. URL: <http://github.com/google/jax>.
- [15] Bui, H.H., Fukagawa, R., Sako, K., Ohno, S., 2008. Lagrangian meshfree particles method (sph) for large deformation and failure flows of geomaterial using elastic-plastic soil constitutive model. *International journal for numerical and analytical methods in geomechanics* 32, 1537–1570.
- [16] Cai, S., Mao, Z., Wang, Z., Yin, M., Karniadakis, G.E., 2021. Physics-informed neural networks (pinns) for fluid mechanics: A review. *Acta Mechanica Sinica* 37, 1727–1738.
- [17] Calvello, M., Cuomo, S., Ghasemi, P., 2017. The role of observations in the inverse analysis of landslide propagation. *Computers and Geotechnics* 92, 11–21.
- [18] Chen, J.S., Hillman, M., Chi, S.W., 2017. Meshfree methods: progress made after 20 years. *Journal of Engineering Mechanics* 143, 04017001.
- [19] Chen, S., Xu, Y., Yu, C., Li, L., Ma, X., Xu, Z., Hsu, D., 2022a. Daxbench: Benchmarking deformable object manipulation with differentiable physics. *arXiv preprint arXiv:2210.13066* .
- [20] Chen, S., Yan, H., Shao, W., Yu, W., Wei, L., Yang, Z., Su, Y., Kan, G., Luo, S., 2022b. Inverse estimation of soil hydraulic parameters in a landslide deposit based on a de-mc approach. *Water* 14, 3693.
- [21] Choi, Y., Kumar, K., 2024. Inverse analysis of granular flows using differentiable graph neural network simulator. *Computers and Geotechnics* 171, 106374.
- [22] Choi, Y., Macedo, J., Liu, C., 2025. Differentiable graph neural network simulator for forward and inverse modeling of multi-layered slope system with multiple material properties. *arXiv preprint arXiv:2504.15938* .
- [23] Courant, R., Friedrichs, K., Lewy, H., 1967. On the partial difference equations of mathematical physics. *IBM journal of Research and Development* 11, 215–234.
- [24] Crosta, G.B., Imposimato, S., Roddeman, D., 2003. Numerical modelling of large landslides stability and runout. *Natural Hazards and Earth System Sciences* 3, 523–538.
- [25] Cundall, P.A., Hart, R.D., 1992. Numerical modelling of discontinua. *Engineering computations* 9, 101–113.
- [26] Cundall, P.A., Strack, O.D., 1979. A discrete numerical model for granular assemblies. *geotechnique* 29, 47–65.

- [27] Cuomo, S., Di Cola, V.S., Giampaolo, F., Rozza, G., Raissi, M., Piccialli, F., 2022. Scientific machine learning through physics-informed neural networks: Where we are and what's next. *Journal of Scientific Computing* 92, 88.
- [28] De Vaucorbeil, A., Nguyen, V.P., Sinaie, S., Wu, J.Y., 2020. Material point method after 25 years: Theory, implementation, and applications. *Advances in applied mechanics* 53, 185–398.
- [29] Deb, R., Jenny, P., 2017. Finite volume-based modeling of flow-induced shear failure along fracture manifolds. *International Journal for Numerical and Analytical Methods in Geomechanics* 41, 1922–1942.
- [30] Demirdžić, I., Muzaferija, S., 1995. Numerical method for coupled fluid flow, heat transfer and stress analysis using unstructured moving meshes with cells of arbitrary topology. *Computer methods in applied mechanics and engineering* 125, 235–255.
- [31] Drucker, D.C., Prager, W., 1952. Soil mechanics and plastic analysis or limit design. *Quarterly of applied mathematics* 10, 157–165.
- [32] Du, H., Guo, B., He, Q., 2024. Differentiable neural-integrated meshfree method for forward and inverse modeling of finite strain hyperelasticity. *Engineering with Computers* , 1–21.
- [33] Du, H., He, Q., 2024. Neural-integrated meshfree (nim) method: A differentiable programming-based hybrid solver for computational mechanics. *Computer Methods in Applied Mechanics and Engineering* 427, 117024.
- [34] Du, H., Zhao, Z., Cheng, H., Yan, J., He, Q., 2023. Modeling density-driven flow in porous media by physics-informed neural networks for co2 sequestration. *Computers and Geotechnics* 159, 105433.
- [35] Gelbrecht, M., White, A., Bathiany, S., Boers, N., 2023. Differentiable programming for earth system modeling. *Geoscientific Model Development* 16, 3123–3135.
- [36] Gill, J.C., Malamud, B.D., 2014. Reviewing and visualizing the interactions of natural hazards. *Reviews of geophysics* 52, 680–722.
- [37] Gingold, R.A., Monaghan, J.J., 1977. Smoothed particle hydrodynamics: theory and application to non-spherical stars. *Monthly notices of the royal astronomical society* 181, 375–389.
- [38] Goswami, S., Anitescu, C., Chakraborty, S., Rabczuk, T., 2020. Transfer learning enhanced physics informed neural network for phase-field modeling of fracture. *Theoretical and Applied Fracture Mechanics* 106, 102447.

- [39] Haghghat, E., Raissi, M., Moure, A., Gomez, H., Juanes, R., 2021. A physics-informed deep learning framework for inversion and surrogate modeling in solid mechanics. *Computer Methods in Applied Mechanics and Engineering* 379, 113741.
- [40] Harlow, F.H., 1964. The particle-in-cell computing method for fluid dynamics. *Methods Comput. Phys.* 3, 319–343.
- [41] He, Q., Barajas-Solano, D., Tartakovsky, G., Tartakovsky, A.M., 2020. Physics-informed neural networks for multiphysics data assimilation with application to subsurface transport. *Advances in Water Resources* 141, 103610.
- [42] He, Q., Perego, M., Howard, A.A., Karniadakis, G.E., Stinis, P., 2023. A hybrid deep neural operator/finite element method for ice-sheet modeling. *Journal of Computational Physics* 492, 112428.
- [43] Heek, J., Levsikaya, A., Oliver, A., Ritter, M., Rondepierre, B., Steiner, A., van Zee, M., 2024. Flax: A neural network library and ecosystem for JAX. URL: <http://github.com/google/flax>.
- [44] Hennigan, T., Cai, T., Norman, T., Martens, L., Babuschkin, I., 2020. Haiku: Sonnet for JAX. URL: <http://github.com/deepmind/dm-haiku>.
- [45] Hidano, S., Pan, S., Yoshida, K., Nomura, R., Miki, Y., Kawai, M., Moriguchi, S., Nakajima, K., Terada, K., 2025. B-spline-based material point method with dynamic load balancing technique for large-scale simulation. *Engineering with Computers* , 1–18.
- [46] Highland, L., 1997. Debris-flow hazards in the United States. volume 176. US Department of the Interior, US Geological Survey.
- [47] Homel, M.A., Herbold, E.B., 2017. Field-gradient partitioning for fracture and frictional contact in the material point method. *International Journal for Numerical Methods in Engineering* 109, 1013–1044.
- [48] Hu, F., Niezgodna, S., Xue, T., Cao, J., 2025. Efficient gpu-computing simulation platform jax-cpfem for differentiable crystal plasticity finite element method. *npj Computational Materials* 11, 46.
- [49] Hu, Y., Anderson, L., Li, T.M., Sun, Q., Carr, N., Ragan-Kelley, J., Durand, F., 2019a. DiffTaichi: Differentiable programming for physical simulation. *arXiv preprint arXiv:1910.00935* .
- [50] Hu, Y., Li, T.M., Anderson, L., Ragan-Kelley, J., Durand, F., 2019b. Taichi: a language for high-performance computation on spatially sparse data structures. *ACM Transactions on Graphics (TOG)* 38, 201.

- [51] Hu, Y., Liu, J., Spielberg, A., Tenenbaum, J.B., Freeman, W.T., Wu, J., Rus, D., Matusik, W., 2019c. Chainqueen: A real-time differentiable physical simulator for soft robotics, in: 2019 International conference on robotics and automation (ICRA), IEEE. pp. 6265–6271.
- [52] Huang, P., Li, S.l., Guo, H., Hao, Z.m., 2015. Large deformation failure analysis of the soil slope based on the material point method. *computational Geosciences* 19, 951–963.
- [53] Huo, Z., Alkhimenkov, Y., Jaboyedoff, M., Podladchikov, Y., Räss, L., Wyser, E., Mei, G., 2025. A high-performance backend-agnostic material point method solver in julia. *Computers and Geotechnics* 183, 107189. URL: <https://www.sciencedirect.com/science/article/pii/S0266352X25001387>, doi:doi:<https://doi.org/10.1016/j.compgeo.2025.107189>.
- [54] Innes, M., Edelman, A., Fischer, K., Rackauckas, C., Saba, E., Shah, V.B., Tebbutt, W., 2019. A differentiable programming system to bridge machine learning and scientific computing. *arXiv preprint arXiv:1907.07587* .
- [55] Jiang, C., Schroeder, C., Selle, A., Teran, J., Stomakhin, A., 2015. The affine particle-in-cell method. *ACM Transactions on Graphics (TOG)* 34, 1–10.
- [56] Kidger, P., Garcia, C., 2021. Equinox: neural networks in JAX via callable PyTrees and filtered transformations. *Differentiable Programming workshop at Neural Information Processing Systems 2021* .
- [57] Klár, G., Gast, T., Pradhana, A., Fu, C., Schroeder, C., Jiang, C., Teran, J., 2016. Drucker-prager elastoplasticity for sand animation. *ACM Transactions on Graphics (TOG)* 35, 1–12.
- [58] Koh, C., Gao, M., Luo, C., 2012. A new particle method for simulation of incompressible free surface flow problems. *International journal for numerical methods in engineering* 89, 1582–1604.
- [59] Kumar, A., Das, P.K., 2023. Experimental and numerical investigation on the collapse of annular columns of dry granular matter. *Powder Technology* 429, 118951.
- [60] Kumar, K., Salmond, J., Kularathna, S., Wilkes, C., Tjung, E., Biscontin, G., Soga, K., 2019. Scalable and modular material point method for large-scale simulations. *arXiv preprint arXiv:1909.13380* .
- [61] Lees, A., 2016. *Geotechnical finite element analysis: a practical guide*. ICE publishing.
- [62] Li, J., Gao, Y., Dai, J., Li, S., Hao, A., Qin, H., 2023a. Mpmnet: A data-driven mpm framework for dynamic fluid-solid interaction. *IEEE Transactions on Visualization and Computer Graphics* .

- [63] Li, J., Hamamoto, Y., Liu, Y., Zhang, X., 2014. Sloshing impact simulation with material point method and its experimental validations. *Computers & Fluids* 103, 86–99.
- [64] Li, X., Qiao, Y.L., Chen, P.Y., Jatavallabhula, K.M., Lin, M., Jiang, C., Gan, C., 2023b. Pac-nerf: Physics augmented continuum neural radiance fields for geometry-agnostic system identification. *arXiv preprint arXiv:2303.05512* .
- [65] Li, Z., Kovachki, N., Azizzadenesheli, K., Liu, B., Bhattacharya, K., Stuart, A., Anandkumar, A., 2020. Fourier neural operator for parametric partial differential equations. *arXiv preprint arXiv:2010.08895* .
- [66] Liang, J., Lin, M., Koltun, V., 2019. Differentiable cloth simulation for inverse problems. *Advances in neural information processing systems* 32.
- [67] Liu, G.R., Liu, M.B., 2003. *Smoothed particle hydrodynamics: a meshfree particle method*. World scientific.
- [68] Lu, L., Jin, P., Pang, G., Zhang, Z., Karniadakis, G.E., 2021. Learning nonlinear operators via deepnet based on the universal approximation theorem of operators. *Nature machine intelligence* 3, 218–229.
- [69] Mistani, P.A., Pakravan, S., Ilango, R., Gibou, F., 2023. Jax-dips: Neural bootstrapping of finite discretization methods and application to elliptic problems with discontinuities. *Journal of Computational Physics* , 112480.
- [70] Molinos, M., Chandra, B., Stickle, M.M., Soga, K., 2023. On the derivation of a component-free scheme for lagrangian fluid–structure interaction problems. *Acta Mechanica* 234, 1777–1809.
- [71] Nakamura, K., Matsumura, S., Mizutani, T., 2023. Taylor particle-in-cell transfer and kernel correction for material point method. *Computer Methods in Applied Mechanics and Engineering* 403, 115720.
- [72] Newbury, R., Collins, J., He, K., Pan, J., Posner, I., Howard, D., Cosgun, A., 2024. A review of differentiable simulators. *IEEE Access* .
- [73] Nguyen, N.H., Bui, H.H., Nguyen, G.D., 2020. Effects of material properties on the mobility of granular flow. *Granular Matter* 22, 59.
- [74] Nübel, K., Huang, W., 2004. A study of localized deformation pattern in granular media. *Computer Methods in Applied Mechanics and Engineering* 193, 2719–2743.
- [75] Pfaff, T., Fortunato, M., Sanchez-Gonzalez, A., Battaglia, P., 2020. Learning mesh-based simulation with graph networks, in: *International conference on learning representations*.

- [76] Potts, D.M., Zdravković, L., Addenbrooke, T.I., Higgins, K.G., Kovačević, N., 2001. Finite element analysis in geotechnical engineering: application. volume 2. Thomas Telford London.
- [77] Rackauckas, C., Ma, Y., Martensen, J., Warner, C., Zubov, K., Supekar, R., Skinner, D., Ramadhan, A., Edelman, A., 2020. Universal differential equations for scientific machine learning. arXiv preprint arXiv:2001.04385 .
- [78] Raissi, M., Perdikaris, P., Karniadakis, G.E., 2019. Physics-informed neural networks: A deep learning framework for solving forward and inverse problems involving nonlinear partial differential equations. *Journal of Computational physics* 378, 686–707.
- [79] Raissi, M., Yazdani, A., Karniadakis, G.E., 2020. Hidden fluid mechanics: Learning velocity and pressure fields from flow visualizations. *Science* 367, 1026–1030.
- [80] Rao, C., Sun, H., Liu, Y., 2021. Physics-informed deep learning for computational elastodynamics without labeled data. *Journal of Engineering Mechanics* 147, 04021043.
- [81] Sanchez-Gonzalez, A., Godwin, J., Pfaff, T., Ying, R., Leskovec, J., Battaglia, P., 2020. Learning to simulate complex physics with graph networks, in: *International conference on machine learning*, PMLR. pp. 8459–8468.
- [82] Sapienza, F., Bolibar, J., Schäfer, F., Groenke, B., Pal, A., Boussange, V., Heimbach, P., Hooker, G., Pérez, F., Persson, P.O., et al., 2024. Differentiable programming for differential equations: A review. arXiv preprint arXiv:2406.09699 .
- [83] Sharabi, O.R., Lewin, S., Louppe, G., 2024. A neural material point method for particle-based simulations, in: *ICML 2024 AI for Science Workshop*. URL: <https://openreview.net/forum?id=sg9Sw1ISQ9>.
- [84] Shen, C., Appling, A.P., Gentine, P., Bandai, T., Gupta, H., Tartakovsky, A., Baity-Jesi, M., Fenicia, F., Kifer, D., Li, L., et al., 2023. Differentiable modelling to unify machine learning and physical models for geosciences. *Nature Reviews Earth & Environment* 4, 552–567.
- [85] Shi, Y., Guo, N., Yang, Z., 2024. Geotaichi: A taichi-powered high-performance numerical simulator for multiscale geophysical problems. *Computer Physics Communications* 301, 109219.
- [86] Sinaie, S., Nguyen, V.P., Nguyen, C.T., Bordas, S., 2017. Programming the material point method in julia. *Advances in Engineering Software* 105, 17–29.

- [87] Staron, L., Hinch, E., 2005. Study of the collapse of granular columns using two-dimensional discrete-grain simulation. *Journal of Fluid Mechanics* 545, 1–27.
- [88] Steffen, M., Kirby, R.M., Berzins, M., 2008. Analysis and reduction of quadrature errors in the material point method (mpm). *International journal for numerical methods in engineering* 76, 922–948.
- [89] Stoker, J.J., 2019. *Water waves: The mathematical theory with applications*. Courier Dover Publications.
- [90] Sulsky, D., Chen, Z., Schreyer, H.L., 1994. A particle method for history-dependent materials. *Computer methods in applied mechanics and engineering* 118, 179–196.
- [91] Sulsky, D., Zhou, S.J., Schreyer, H.L., 1995. Application of a particle-in-cell method to solid mechanics. *Computer physics communications* 87, 236–252.
- [92] Toshev, A.P., Ramachandran, H., Erbesdobler, J.A., Galletti, G., Brandstetter, J., Adams, N.A., 2024. Jax-sph: A differentiable smoothed particle hydrodynamics framework. *arXiv preprint arXiv:2403.04750* .
- [93] Wang, D., Bienen, B., Nazem, M., Tian, Y., Zheng, J., Pucker, T., Randolph, M.F., 2015. Large deformation finite element analyses in geotechnical engineering. *Computers and geotechnics* 65, 104–114.
- [94] Wang, S., Teng, Y., Perdikaris, P., 2021. Understanding and mitigating gradient flow pathologies in physics-informed neural networks. *SIAM Journal on Scientific Computing* 43, A3055–A3081.
- [95] Wood, D.M., 1990. *Soil behaviour and critical state soil mechanics*. Cambridge university press.
- [96] Xu, J., Chen, T., Zlokapa, L., Foshey, M., Matusik, W., Sueda, S., Agrawal, P., 2021. An end-to-end differentiable framework for contact-aware robot design. *arXiv preprint arXiv:2107.07501* .
- [97] Xu, W., Zheng, D., Li, Y., Ren, J., Lu, C., 2024. Differentiable fluid physics parameter identification by stirring and for stirring, in: *2024 IEEE/RSJ International Conference on Intelligent Robots and Systems (IROS)*, IEEE. pp. 11624–11630.
- [98] Xue, T., Liao, S., Gan, Z., Park, C., Xie, X., Liu, W.K., Cao, J., 2023. Jax-fem: A differentiable gpu-accelerated 3d finite element solver for automatic inverse design and mechanistic data science. *Computer Physics Communications* , 108802.

- [99] Yin, M., Zhang, E., Yu, Y., Karniadakis, G.E., 2022. Interfacing finite elements with deep neural operators for fast multiscale modeling of mechanics problems. *Computer methods in applied mechanics and engineering* 402, 115027.
- [100] Yuan, B., Choo, C.S., Yeo, L.Y., Wang, Y., Yang, Z., Guan, Q., Suryasentana, S., Choo, J., Shen, H., Megia, M., et al., 2025. Physics-informed machine learning in geotechnical engineering: a direction paper. *Geomechanics and Geoengineering* , 1–32.
- [101] Yuhn, C., Sato, Y., Kobayashi, H., Kawamoto, A., Nomura, T., 2023. 4d topology optimization: Integrated optimization of the structure and self-actuation of soft bodies for dynamic motions. *Computer Methods in Applied Mechanics and Engineering* 414, 116187.
- [102] Zhang, X., Chen, Z., Liu, Y., 2016. *The material point method: a continuum-based particle method for extreme loading cases*. Academic Press.
- [103] Zhao, H., Kowalski, J., 2022. Bayesian active learning for parameter calibration of landslide run-out models. *Landslides* 19, 2033–2045.
- [104] Zhu, Y., Bridson, R., 2005. Animating sand as a fluid. *ACM Transactions on Graphics (TOG)* 24, 965–972.